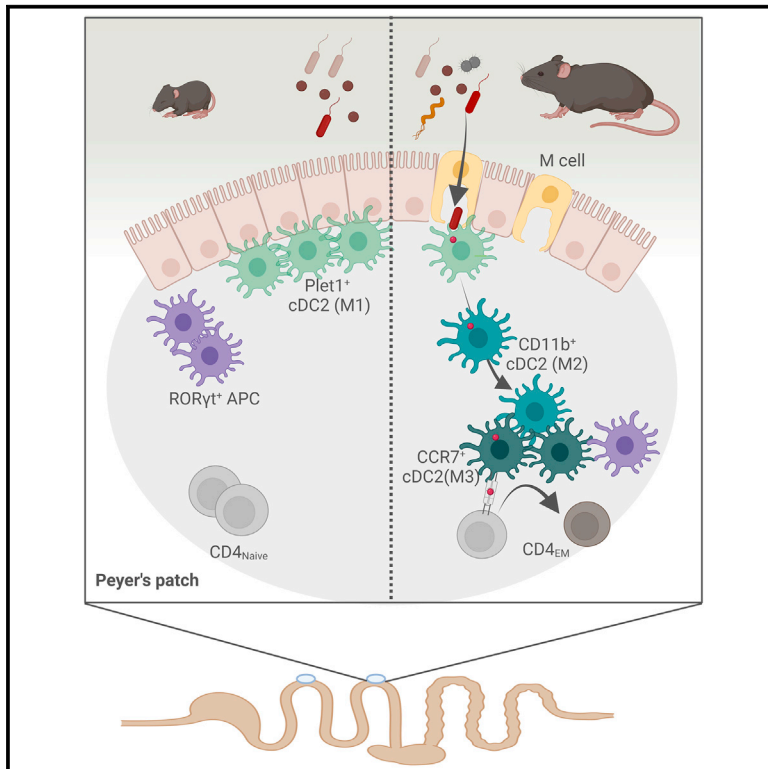# Immunity

M cell maturation and cDC activation determine the onset of adaptive immune priming in the neonatal Peyer's patch

Graphical abstract

Authors

Natalia Torow, Ronghui Li,
Thomas Charles Adrian Hitch, ...,
Hugues Lelouard, Ivan Gesteira Costa,
Mathias Walter Hornef

Correspondence

ntorow@ukaachen.de (N.T.),
mhornef@ukaachen.de (M.W.H.)

In brief

Despite the critical importance of immune development in early life, our mechanistic understanding of this process is limited. Torow et al. demonstrate that postnatal establishment of intestinal microbe-host interaction is not expressly driven by early microbial colonization, but rather the maturation of Peyer's patch M cells and antigen-presenting cells.

Highlights

- Peyer's patch (PP) CD4^{+} T cells exhibit delayed maturation after birth

- cDC1 and RORgt^{+} APC are increased whereas cDC2 are diminished in the neonatal PP

- PP APCs exhibit halted maturation and cDC2 show reduced T cell priming capacity

- M cell development is required and sufficient to drive APC maturation

CellPress

Article

M cell maturation and cDC activation determine the onset of adaptive immune priming in the neonatal Peyer's patch

Natalia Torow,[1,*] Ronghui Li,[2,17] Thomas Charles Adrian Hitch,[3] Clemens Mingels,[1,18] Shahed Al Bounny,[1]
Niels van Best,[1,4] Eva-Lena Stange,[1] Britta Simons,[5] Tiago Maié,[2] Lennart Rüttger,[1,19]
Narasimha Murthy Keshava Prasad Gubbi,[1] Darryl Adelaide Abbott,[6] Adam Benabid,[7] Michael Gadermayr,[8,20]
Solveig Runge,[9,10] Nicole Treichel,[1] Dorit Merhof,[8,21] Stephan Patrick Rosshart,[9,11] Nico Jehmlich,[12]
Timothy Wesley Hand,[6] Martin von Bergen,[12,15,16] Felix Heymann,[13] Oliver Pabst,[5] Thomas Clavel,[3] Frank Tacke,[13]
Hugues Lelouard,[14] Ivan Gesteira Costa,[2] and Mathias Walter Hornef[1,22,*]

[1]Institute of Medical Microbiology, RWTH Aachen University Hospital, Aachen 52074, Germany
[2]Institute for Computational Genomics, RWTH Aachen University Hospital, Aachen 52074, Germany
[3]Functional Microbiome Research Group, Institute of Medical Microbiology, RWTH Aachen University Hospital, Aachen 52074, Germany
[4]Department of Medical Microbiology, School of Nutrition and Translational Research in Metabolism (NUTRIM), Maastricht University, Maastricht 6200, the Netherlands
[5]Institute of Molecular Medicine, RWTH Aachen University Hospital, Aachen 52074, Germany
[6]Pediatrics Department, UPMC Children's Hospital of Pittsburgh, University of Pittsburgh School of Medicine, Pittsburgh, PA 15224, USA
[7]Institute for Cell and Tumor Biology, RWTH Aachen University Hospital, Aachen 52074, Germany
[8]Institute of Imaging & Computer Vision, RWTH Aachen University, Aachen 52056, Germany
[9]Department of Microbiome Research, Friedrich-Alexander-University Erlangen-Nürnberg, Erlangen 91054, Germany
[10]Faculty of Biology, University of Freiburg, Freiburg im Breisgau, Germany
[11]Department of Medicine II, University of Freiburg, Freiburg im Breisgau, Germany
[12]Helmholtz-Centre for Environmental Research GmbH – UFZ, Department of Molecular Systems Biology, Leipzig 04318, Germany
[13]Department of Hepatology & Gastroenterology, Charité University Hospital, Berlin 13353, Germany
[14]Aix Marseille University, CNRS, INSERM, CIML, Marseille 13288, France
[15]German Centre for Integrative Biodiversity Research (iDiv), Leipzig 04103, Germany
[16]University of Leipzig, Faculty of Life Sciences, Institute of Biochemistry, Leipzig 04103, Germany
[17]Present address: Department of Emergency Medicine, Qilu Hospital of Shandong University, Jinan, China
[18]Present address: Departement of Nuclear Medicine, Inselspital, Bern University Hospital, University of Bern, Bern, Switzerland
[19]Present address: Würzburg Institute of Systems Immunology, Julius-Maximilians-Universität, Würzburg 97072, Germany
[20]Present address: Department of Information Technology and Systems Management, Salzburg University of Applied Sciences, Salzburg, Austria
[21]Present address: Institute of Image Analysis and Computer Vision, University of Regensburg, Regensburg 93063, Germany
[22]Lead contact
*Correspondence: ntorow@ukaachen.de (N.T.), mhornef@ukaachen.de (M.W.H.)
https://doi.org/10.1016/j.immuni.2023.04.002

SUMMARY

Early-life immune development is critical to long-term host health. However, the mechanisms that determine the pace of postnatal immune maturation are not fully resolved. Here, we analyzed mononuclear phagocytes (MNPs) in small intestinal Peyer's patches (PPs), the primary inductive site of intestinal immunity. Conventional type 1 and 2 dendritic cells (cDC1 and cDC2) and RORgt+ antigen-presenting cells (RORgt+ APC) exhibited significant age-dependent changes in subset composition, tissue distribution, and reduced cell maturation, subsequently resulting in a lack in CD4+ T cell priming during the postnatal period. Microbial cues contributed but could not fully explain the discrepancies in MNP maturation. Type I interferon (IFN) accelerated MNP maturation but IFN signaling did not represent the physiological stimulus. Instead, follicle-associated epithelium (FAE) M cell differentiation was required and sufficient to drive postweaning PP MNP maturation. Together, our results highlight the role of FAE M cell differentiation and MNP maturation in postnatal immune development.

INTRODUCTION

The neonatal immune system differs in many aspects from the adult in both mice and men. This reflects the ongoing tissue development and stepwise processes that ultimately establish the self-controlled adaptive immune system.[1,2] However, even though post-natal immune maturation impacts life-long host-microbial homeostasis and health, the mechanisms
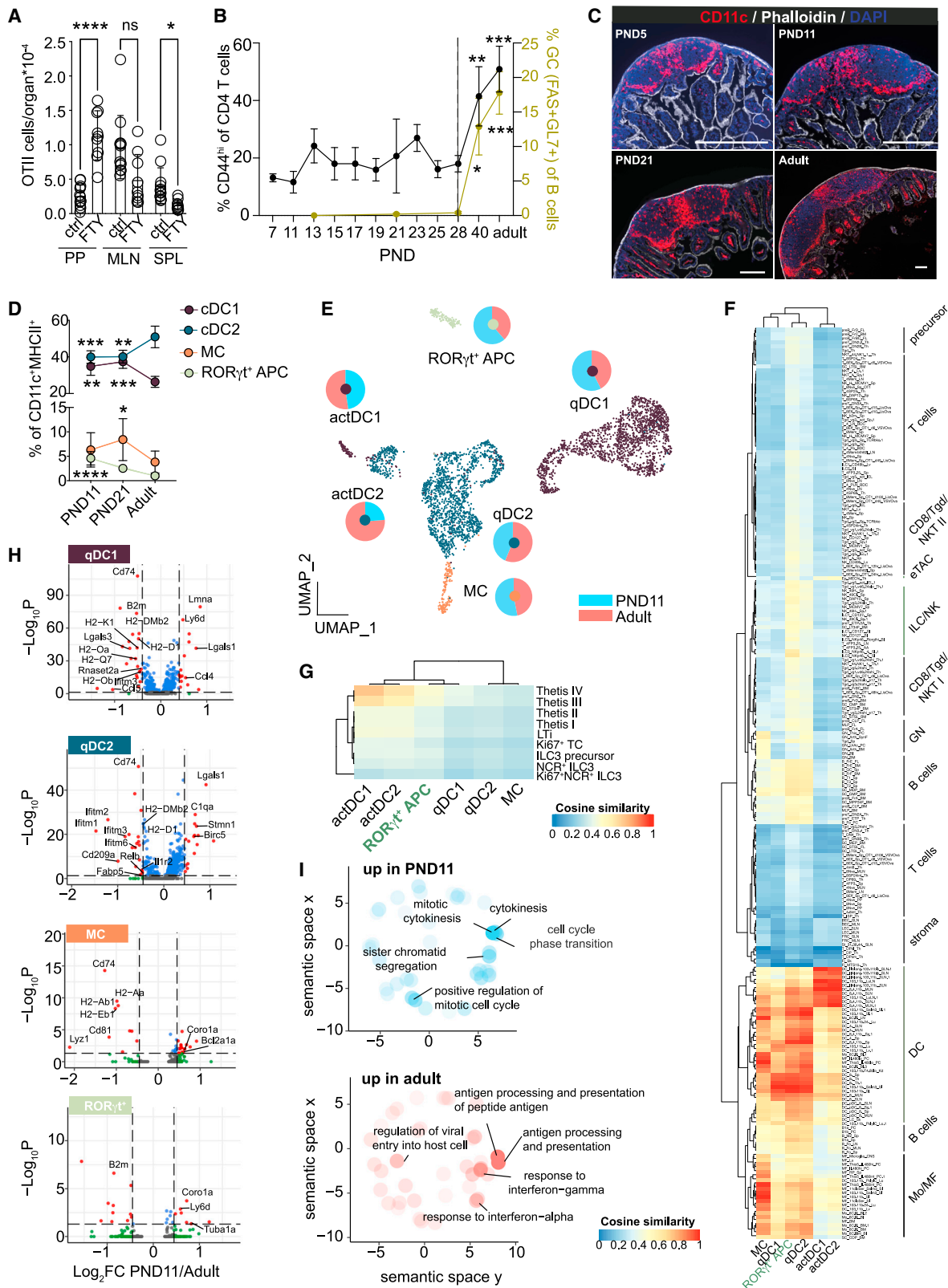
Figure 1. Neonatal PP MNPs exhibit diminished antimicrobial activity and reduced antigen processing and presentation capacity
(A) OTII cell numbers (PP, Peyer's patch; MLN, mesenteric lymph node; SPL, spleen) of PND10 mice administered with OVA ± FTY720 on PND 6–8 (n = 9–13, mean, one-way ANOVA/Kruskall-Wallis test).

determining mucosal immune maturation are incompletely understood.

Early-life developmental processes contribute to cell homing and differentiation, tissue microarchitecture, and organ function. Environmental cues mainly represented by microbiota-derived signals stimulate immune maturation and reinforce mucosal barrier integrity.[3] They play a protective role in various immune-mediated diseases in mice[4-7] and humans.[8-10] Microbial proteins represent the main source of immunogenic antigens since breast-milk proteins represent self-antigen. Endogenous mediators such as type I interferon (IFN) alter the basal state of immune cells,[11] induce cell maturation,[12] augment endocytic and proteolytic activity, increase antigen cross-presentation capacity[11,13-15] and enhance adaptive immunity.[16,17] The role of endogenous mediators and microbial stimuli for post-natal immune maturation and the spectrum of immunogenic antigens at the neonatal inductive sites remain ill-defined.

Small intestinal (SI) Peyer's patches (PPs) represent a main mucosal inductive site and anatomical place of early T cell homing in the murine mucosa.[18] In the adult host, microfold (M) cells as integrative part of the PP follicle-associated epithelium (FAE) sample antigen directly from the SI lumen and transfer it to subepithelial antigen-presenting cells (APCs) that are arrayed in an intricate microarchitecture in the subepithelial dome (SED) and the interfollicular region (IFR) where they prime T cells.[19] T cell priming in turn aids B cell activation and IgA production, a fundamental feature of host-microbial homeostasis in the intestine.[20,21] The intense and continuous interaction between gut luminal stimuli and the mucosal immune system under homeostatic conditions explains the extraordinarily high frequency of antigen-experienced CD4+ T cells and germinal center B cells in adult PP. The frequency of mature T cells is markedly lower in neonatal PP and this remains unchanged for a prolonged time after birth despite their principal functionality.[18] Although post-natal maturation of the PP mononuclear phagocyte (MNP) compartment has not been systematically investigated, recent work highlighted the presence of non-conventional APCs in the murine mesenteric lymph node (MLN). Beside type 3 innate lymphoid cell (ILC) APCs that were required for regulatory T cell maturation in the MLN, distinct clusters of RORγt+MHCII+, so called Thetis cells (TCs), were described, which exhibited a non-redundant functional role during early life.[22-24]

Here, we investigated cellular mechanisms in early life initiating PP homeostatic immune responsiveness. We hypothesized that APCs represent key determinants of this process and analyzed subset composition, anatomical organization, maturation trajectories, tissue environment, and functional profile of neonatal PP MNP. Beside the type 1 and 2 conventional dendritic cells (cDCs) and monocyte-derived MNPs (monocyte-derived cell [MC]), we identified and characterized a population of RORγt+ APC. We also investigated the influence of the early enteric microbiota, the spectrum of available antigens and type I IFN on APC maturation and T cell priming. Finally, we studied the post-natal differentiation of M cells within the FAE overlaying PP and translocation of luminal particulate antigen. Our results suggest that post-natal FAE M cell differentiation determines the onset of APC maturation and functionality as well as intestinal immune homeostasis. A better understanding of immune priming in early life may aid to unravel the functional importance of this critical time window for immune homeostasis and ultimately allow manipulation of immune effector function in the neonatal host.

RESULTS

Reduced number and antigen presentation capacity of cDC2

Thymic output in the murine host is initiated around birth and homing of T cells to the neonatal intestinal lymphoid tissue occurs independent of signals from the enteric microbiota (Figure S1A). To determine the immune reactivity of enteric lymphoid tissues to mucosal antigen exposure in the neonatal setting, we transferred OTII cells into neonatal animals and orally administered OVA in presence or absence of FTY720, an inhibitor of lymphocyte egress. FTY720 treatment enriched OTII cells in PP, suggesting that they represent a primary site of early-life immune reactivity (Figure 1A). Nevertheless, under homeostatic conditions the percentage of CD44hi CD4+ T cells in PP remained low throughout the post-natal period. In contrast, in adult PP, >50% of CD4+ T cells were CD44hi, reminiscent of an activated phenotype. T cell activation increased after 4 weeks of age, concordant with increased FAS+GL7+ germinal center B cells (Figure 1B).

Given the central role of MNPs in antigen processing, environmental and microbial signal integration, and T cell priming, we next compared the localization and transcriptional profile of PP MNP between neonatal and adult mice. To avoid problems linked to cell isolation from small sized tissue samples, we first measured the strength and distribution of the pan-phagocyte marker CD11c normalized to the area of the patch. The total phagocyte density was not reduced in neonatal (post-natal day [PND]5 and PND11) vs. weanling (PND21) or adult PP (Figures 1C and S1B). Next, we analyzed PP MNP by flow cytometry to identify age-dependent differences in the subset composition of the various MNP (Figures 1D and S1C).[25] Whereas cDC2s were the dominant MNP subset in adult PP in neonatal PP, cDC2 were reduced, while cDC1 were enriched. RORγt+ APC have been described in the neonatal

(B) Percentage of CD44hi of PP CD4+ T cells (left y axis, black line) and GC B cells of B cells (right y axis, yellow green line) (n = 4–20, mean + SD, one-way ANOVA/Kruskal-Wallis test).

(C) Representative immunofluorescent images of PP stained for CD11c (red), phalloidin (white), DAPI (blue); scale bars, 200 μm.

(D) Percentage of PP MNP subsets (cDC1 = XCR1+SIRPα−MHCII+CD11c+, cDC2 = SIRPα+/hiBST2−XCR1−MHCII+CD11c+, Rorγt+ APC = RORγt+SIRPαloXCR1−MHCII+CD11c+, MC = BST2+SIRPα+XCR1−MHCII+CD11c+) quantified by FACS (n = 5–12, mean + SD; one-way ANOVA/Kruskall-Wallis test).

(E) scRNA-seq of PP MNP (n = 2; pooled from PP from 1 L or 3 adult animals per sample). Pie charts depict relative contribution of PND11 and adult cells within the indicated subset.

(F and G) Pseudobulk profile comparison of scRNA-seq clusters from (D) against (F) all ImmGen gene expression profiles and (G) scRNA-seq of RORγt+MHCII+ cells from Akagbosu et al.[24] using a cosine similarity metric.

(H) DE genes in CCR7− qDC1, CCR7− qDC2, MC, and RORγt+ APC between PND11 and adult mice.

(I) GO terms overrepresented in qDC2 of PND11 (upper panel, blue circles) or adult (lower panel, red circles). Top 5 GO terms are labeled. See also Figure S1.
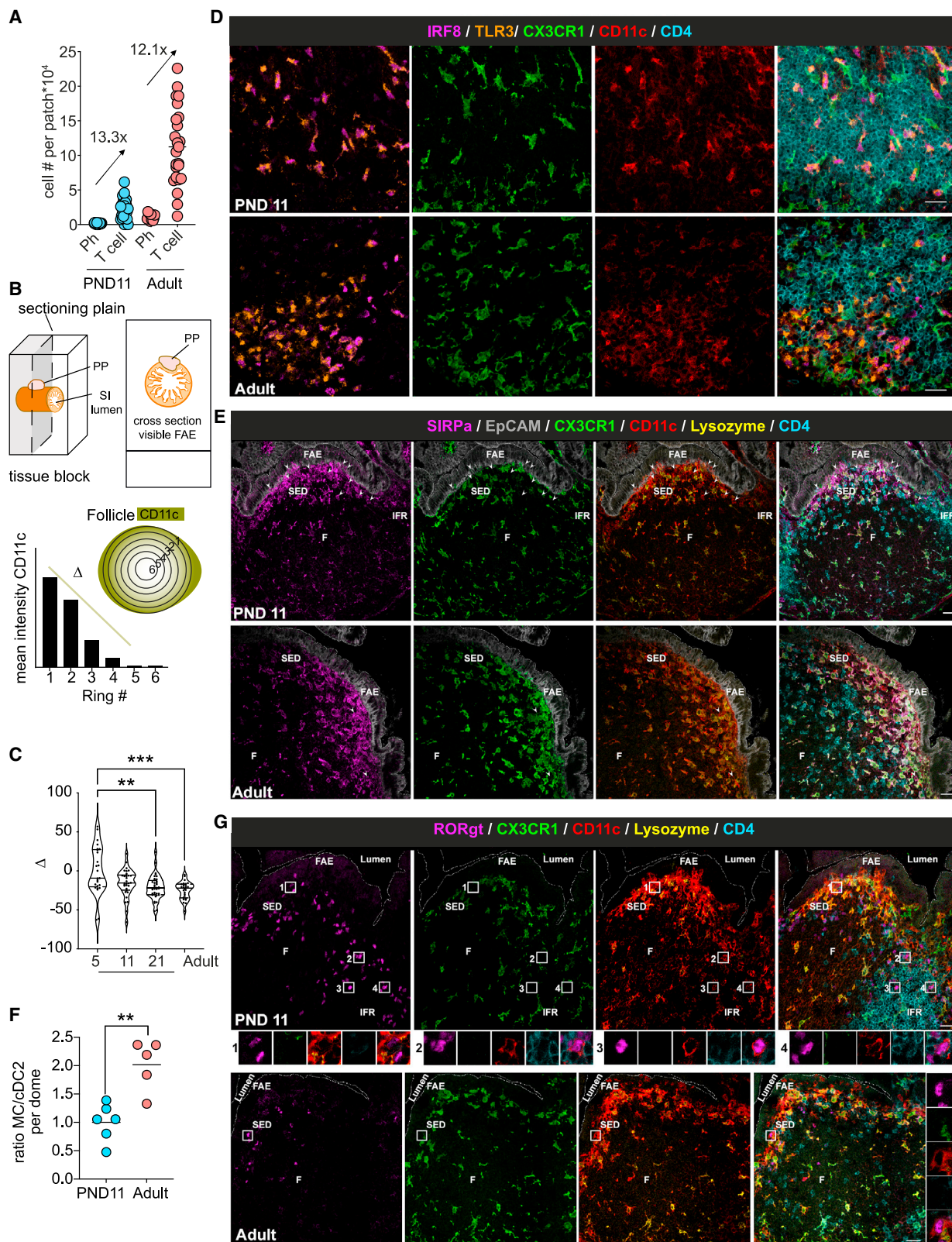
Figure 2. Anatomical distribution of MNPs in neonatal and adult PP

(A) FACS quantification of CD4^{+} T cells and phagocytic cells in PP. Ratio of mean T cell:phagocyte is indicated.

(B) Sample preparation and signal distribution model of CD11c using radial segmentation of the PP to obtain Δ.

spleen (SPL) and MLNs.[24,26,27] We detected RORγt[+−] SIRPα^{lo}XCR1^{−}MHCII^{+}CD11c^{+} APC in PP, which we refer to as RORγt^{+}APC. The frequency of this subset was elevated in early life. The percentage of MCs had similar proportions at PND11 compared with the adult (Figure 1D). Similar age-dependent differences in the MNP subset composition were not observed in *lamina propria* APCs and no significant numbers of RORγt[+] APC were detected (Figure S1D, data not shown).

Additionally, we sorted PP MNP from neonatal (PND11) and adult mice and performed single-cell RNA sequencing (scRNA-seq) to identify age-dependent differences in the transcriptional profile of the various PP MNP subsets. The UMAP revealed six major distinct clusters, of which five were assigned to cDC1, cDC2, or MCs based on known marker genes of cDCs and monocyte-derived APCs (Figures 1E and S1E). The sixth cluster was identified as RORγt[+] APC. The scRNA-seq analysis confirmed age-dependent changes in the MNP subset composition observed by flow cytometry with a higher frequency of cDC1 and RORγt[+] APC and reduced proportion of cDC2 in the neonatal host (Figure 1E). cDC1 and cDC2 each formed two separate clusters representing immature/quiescent (q) and mature/activated (act) CCR7^{+} DC.[28] The transcriptional profiles of qDC1 and qDC2 were distinct from each other and were identified by the expression of the hallmark genes *Sirpa* and *Xcr* (Figures 1E and S1F). As previously described, the homeostatic maturation process was accompanied by substantial transcriptional changes leading to the distinct clustering of actDC from the corresponding qDC counterparts and substantial reduction of the DC lineage-defining genes *Sirpa* and *Xcr1*.[29,30] In addition, homeostatically activated DCs were characterized by expression of a discrete set of genes that was largely overlapping between actDC1 and actDC2 consistent with their functional commitment. Nevertheless, expression of *Cd8a* and *Cst3* remained detectable in actDC1, albeit at lower levels than in qDC1, whereas *S100a4*, *S100a6*, *Klrd1*, and *H2-DMb2* expressed in qDC2 were reduced but remained detectable in actDC2 (Figures 1E, S1E, and S1F). To further confirm our annotation of cDC subsets, we compared the top differentially expressed genes between qDC and actDC identified in Figure S1F with the previously published definition of a core transcriptome of homeostatically quiescent vs. activated cDC from skin, lung, and thymus.[30] The majority of differentially expressed genes identified in PP cDC subsets was also found in the respective qDC vs. actDC core transcriptome and the expression profile was almost identical.

To better understand the nature of RORγt[+] APC, we first compared the six clusters identified in Figure 1E with the gene expression profiles of cells available on ImmGen (Figure 1F). Of all the queried ImmGen cell types, the RORγt[+] APC transcriptional profile showed the greatest similarity to DCs and particu-

larly to the intestinal *lamina propria* cDC2s. The correlation profile of RORγt[+] APC and qDC2 in our dataset to the ImmGen transcriptomes was very similar indicating their transcriptional similarity. RORγt[+]MHCII[+] antigen-presenting TCs were suggested to be enriched in the gut draining lymph node of young mice and to be distinct from type 3 ILCs (ILC3s).[24] We compared our six cell clusters to the published scRNA-seq data of RORγt[+−] MHCII^{+} cells representing Thetis I–IV subsets and ILC3 subsets isolated from PND14 MLN.[24] Overall, CCR7^{+} subsets (actDC1, actDC2, TCIII, and TCIV) showed the greatest similarity to one another reflecting similar general functionality of CCR7^{+} activated/mature cells. PP RORγt[+] APC displayed an intermediate similarity to TCIII and IV and low similarity to antigen-presenting ILC3 cells (Figure 1G).

Comparative analysis of the transcriptional profiles of the MNP subsets revealed that genes involved in (1) antigen presentation and processing (e.g., *Cd74*, *H2-Eb1*, *H2-Dmb2*, *H2-Aa*, *H2-Ab1*, and *H2-K1*), (2) microbicidal activity (e.g., *Rnaset2a* and *Lyz1*), and (3) IFN I signaling (e.g., *Ifitm1*, *Ifitm2*, and *Ifitm3*) had decreased expression in neonatal subsets compared with their adult counterparts (Figure 1H). Neonatal MNP were enriched in transcripts associated with stemness (*Lgals1* and *Birc5*). Both actDC1 and actDC2 were transcriptionally similar between PND11 and adult within the subset (Figure S1H). The altered expression profile of CD74, H2-K1, and lysozyme on protein level was confirmed by FACS (Figure S1I). Consistently, gene ontology (GO) enrichment analysis confirmed that GO terms associated with antigen processing and presentation but also response to IFN I and II were underrepresented in neonatal cells, whereas cell division and morphology-associated pathways were overrepresented compared with adult mice (Figure 1I). Together, these results demonstrate an increase of cDC1 and RORγt[+] APC and reduction of cDC2 in neonatal PP and indicate an overall lower capacity for antigen processing/presentation.

Enrichment of cDC2 at the PP SED

Functional changes of neonatal PP MNPs could be due to altered tissue organization and cellular interaction. Both, overall anatomical MNP distribution or the T cell-to-phagocyte ratio would influence the stochastic probability of T cells recognizing their cognate antigen and could explain the observed lack of homeostatic T cell activation. Quantitative flow cytometric analysis of the ratio of antigen-presenting MHCII^{+}CD11c^{+} cells and CD4^{+} T cells in PP did not reveal any difference between PND11 and adult mice (Figure 2A). Also, the overall MNP tissue distribution showed no age-dependent phenotype. Radial segmentation in adult PP revealed a CD11c signal enriched toward the outer edges of PP that accommodate the SED and IFR, as well as the serosal side of the follicle leading to a negative slope of the line displaying radial (circumferential to central) signal intensity

---

(C) Δ calculated in individual PP (n = 25–36 follicles, Kruskall-Wallis test).

(D, E, and G) Representative spectral confocal imaging projection of PP illustrating anatomical distribution of (D) TLR3^{+}IRF8^{+}CD11c^{+}CX3CR1^{−} cDC1 (TLR3, orange; IRF8, magenta; GFP, green; CD11c, red; CD4, blue [only TLR3^{+} IRF8^{+} cells represent cDC1]), (E) SIRPα^{+}CD11c^{+}CX3CR1^{−}lysozyme^{−} cDC2 (SIRPα, magenta; EpCAM, gray; GFP, green; CD11c, red; lysozyme, yellow; CD4, blue [arrowheads point toward cDC2 in the SED]) and (G) RORγt^{+}CD11c[+−] CX3CR1^{−}CD4^{−} APC (RORγt, magenta; GFP, green; CD11c, red; lysozyme, yellow; CD4, blue [boxed areas of individual RORγt^{+}APC shown below]). Scale bars, 20 μm.

(F) Ratio between SIRPα^{+}CX3CR1^{+}Lysozyme^{+}CD11c^{+} MC and SIRPα^{+}CX3CR1^{−}lysozyme^{−}CD11c^{+} cDC2 in SED shown in (E). (n = 5–6, median, Mann-Whitney U test.) Each dot represents one animal (A) or one follicle (C and G). See also Figure S2.
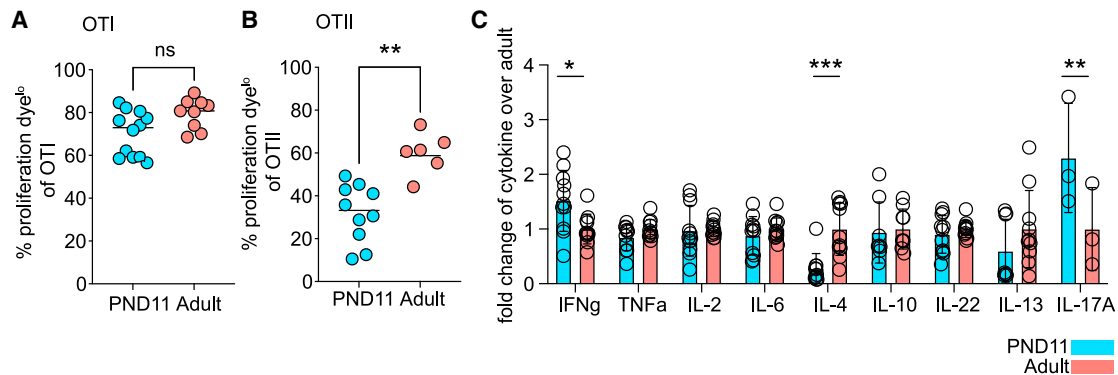
Figure 3. Altered T cell priming by neonatal PP MNPs
(A and B) Proliferation of transferred (A) OTI and (B) OTII cells in PP 48 h after oral OVA (n = 3–11, mean, Mann-Whitney U test).
(C) T helper cytokine levels in the supernatant of OTII and PP MNP co-cultures in presence of OVA (n = 3–11, mean + SD, two-way ANOVA/Sidak's multiple comparison test). See also Figure S3.

(Figure 2B). The mean slope (Δ) was neutral at PND5 indicating a somewhat more equal distribution of CD11c$^+$ cells in PP during the first week of life but became and remained negative after that, suggesting an overall adult-like anatomical distribution of CD11c$^+$ cells from PND11 onward (Figure 2C). However, MNP subsets display a sophisticated anatomical organization in the adult PP.[31] We therefore additionally employed confocal spectral immunofluorescence microscopy to dissect the microarchitecture and tissue distribution of different MNP subtypes. Similar to adults, cDC1 localized mainly to the IFR in the neonatal PP (Figures 2D and S2A). In contrast, marked differences in the MNP distribution between neonatal and adult mice were found in the SED and FAE (Figure 2E). cDC2 were more abundant in the FAE of neonatal mice. Also, they were not restricted to the edge of the SED but present in high numbers at the middle top of the SED in neonatal mice (PND11) interacting intensely with the epithelium (Figures 2E, 2G, S2A, and S2B). Inversely, mococyte-derived lysozyme-expressing (lyso)MNP were more dominant in the adult SED. This resulted in an increased cDC2:lysoMNP ratio in the neonatal SED (Figure 2F). RORγt$^+$ APC in PP of neonatal mice localized both to SED and IFR suggesting a maturation/migration pattern similar to cDC2 (Figures 2G and S2B). Taken together, despite a similar MNP/CD4$^+$ T cell ratio and overall distribution, cDC2 were enriched at the SED and RORγt$^+$ APC in the SED and IFR in the neonate.

**Reduced CD4$^+$ T cell priming in neonatal PP**
Next, we functionally evaluated priming of CD4$^+$ and CD8$^+$ T cells by neonatal PP MNP.[26,28] Therefore, we transferred proliferation dye-labeled TCR-transgenic CD4$^+$ (OTII) or CD8$^+$ (OTI) T cells into neonatal and adult recipients and proliferation was assessed 48 h after oral OVA administration (Figures 3A and 3B). Efficient CD8$^+$ T cell priming was observed both in neonatal and adult PP (Figure 3A). In contrast, CD4$^+$ T cell priming was impaired in neonatal animals (Figure 3B). Also, we assessed the priming capacity of PP MNP toward different T helper subsets *in vitro* by co-culturing sort-purified CD11c$^+$MHCII$^+$ PP MNP with OTII cells and measuring secreted T helper cytokines in the supernatant. OTII cells co-cultured with neonatal PP MNP secreted enhanced levels of IFNγ and IL-17A consistent with our

observation of increased cDC1 and RORγt$^+$ APC numbers in neonatal PP but decreased levels of IL-4 (Figures 3C and S3). These results show that soluble antigen was cross-presented to neonatal PP CD8$^+$ T cells with adult-like efficiency. In contrast, an overall decreased conventional major histocompatibility class (MHC)II presentation of soluble antigen and subsequent CD4$^+$ T cell priming was observed in neonatal mice associated with significant alterations in the spectrum of secreted T helper cytokines.

Microbiota-derived signals promote cDC2 and RORγt$^+$ APC maturation
Changes in the transcriptional profile, anatomical localization, and function of PP MNP in the neonate may reflect alterations in cellular maturation.[25] We analyzed the maturation profile of PP MNP during the post-natal period by generating pseudotime trajectories. The trajectory seed branch was determined by high expression of cell cycling genes and the marker gene of progenitor-like cells *Birc5*. The relative contribution of neonatal cells to the pseudotime trajectory of cDC1 was comparable to that of adult cells suggesting a similar pace of maturation (Figure S4A). In line with that the proportion of CCR7$^+$ actDC1 determined by FACS, albeit low in general, was not altered (Figure S4B). In contrast, the relative contribution of neonatal cells to the pseudotime trajectory of cDC2 steadily decreased with advancing degree of maturation (Figure 4A). Pseudotime analysis and sub-clustering of the cDC2 identified *Birc5*, *Ccr6*, *Plet1*, *Itgam* (encoding CD11b), and *Ccr7* as key marker genes of cDC2 maturation stages (Figure 4B). We then studied cell maturation by flow cytometry utilizing Plet1 (maturation state [M] 1), CD11b (M2), and CCR7 (M3) as markers for the last three successive developmental stages in the life cycle of PP cDC2 (Figure 4C). Comparing those cDC2 developmental stages between PND11 and adult animals, we detected marked differences with an increased proportion of cells in the M1 state but decreased levels of M2 and M3 in the neonate (Figure 4D). Again, this indicated skewing toward a maturational delay of neonatal cDC2. Pseudotime analysis revealed an early maturational delay of neonatal cells also for RORγt$^+$ APC, with neonatal cells enriched at early
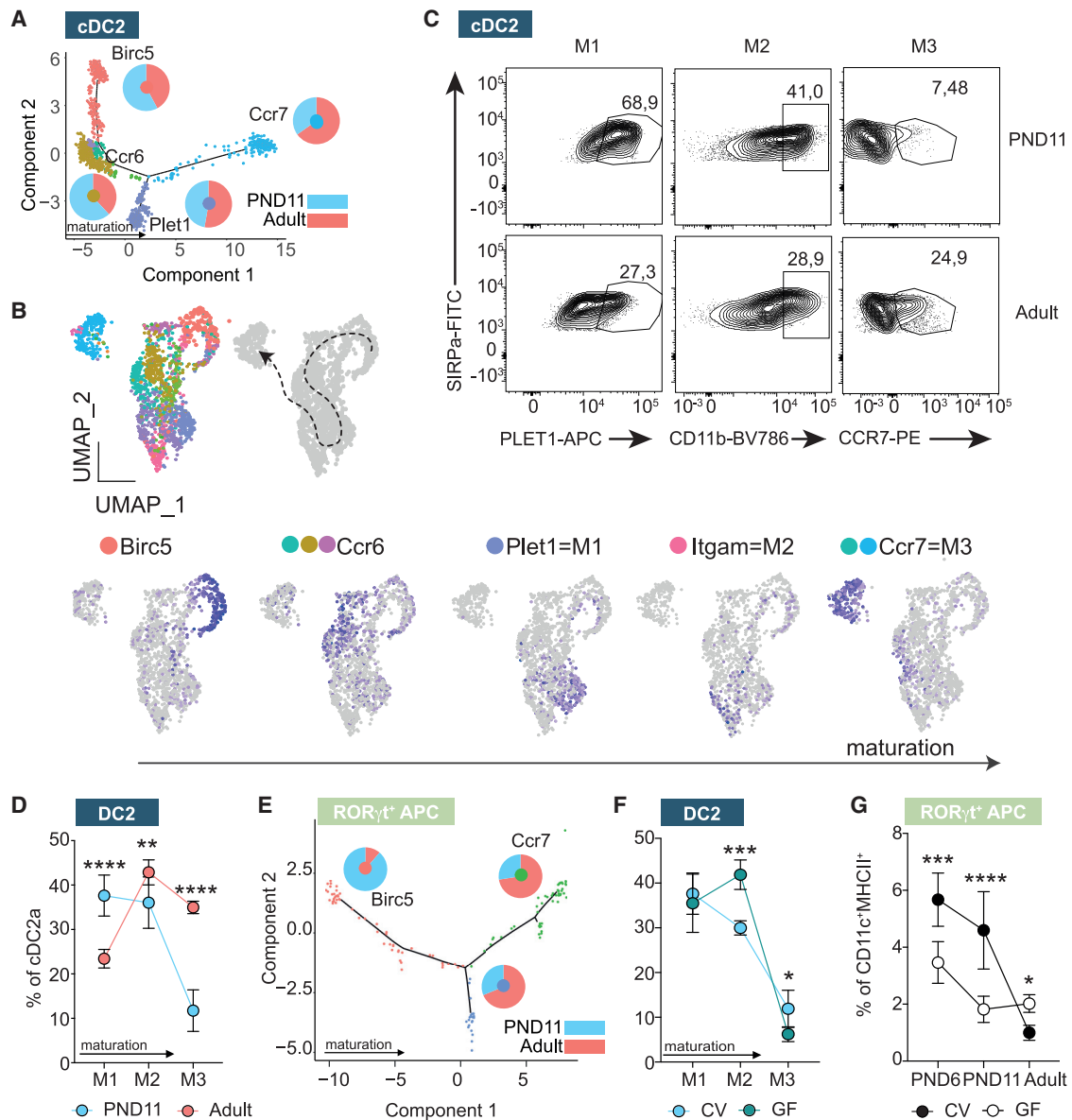
Figure 4. Maturation delay of PP cDC subsets during the post-natal period

(A) cDC2 pseudotime trajectory; pie charts indicate relative contribution of adult and PND11 cells to specific branch; genes indicate marker genes in and color code is consistent with (B).

(B) Seurat subclusters contributing to cDC2 (upper left, subclustered from Figure 1E), proposed maturation trajectory (upper right) and marker genes for maturational stages of cDC2 (bottom).

(C) Representative FACS plots of PP cDC2 showing the expression of PLET1, CD11b, and CCR7 for maturational stages M1, M2, and M3, respectively.

(D) Percentage of M1–M3 cDC2 (n = 8–10, mean + SD, two-way ANOVA/Bonferroni test between age groups within the same maturational stage).

(E) RORgt[+] APC pseudotime trajectory; pie charts indicate relative contribution of adult and PND11 cells to specific branches.

(F) Percentage of M1–M3 of cDC2 in PND11 germ-free (GF) vs. conventional (CV) animals (n = 4–12, mean + SD; two-way ANOVA/Bonferroni test, statistical significance between colonization groups within the same maturational stage) determined by FACS.

(G) Percentage of RORgt[+]APC in germ-free (GF) vs. conventional (CV) animals (n = 4–11, mean + SD, one-way ANOVA/Kruskall-Wallis test, statistical significance indicated within the same age group). See also Figure S4.

differentiation stages (Birc5^{+}) and reduced in the mature/activated subset (Ccr7^{+}) (Figure 4E).

We next asked whether microbial cues contributed to the post-natal MNP maturation and the detected age-related differences.[32] The number of CCR7^{+} migratory cDC1 was indepen-

dent of the presence of viable microbiota (Figure S4C). In contrast, cDC2 of germ-free (GF) PND11 mice were increased proportionally in the M2 state (CD11b^{+}) but decreased in M3 (CCR7^{+}) suggesting that microbial signals contributed to the final maturation step of cDC2 from M2 to M3 (Figure 4F). cDC2 were
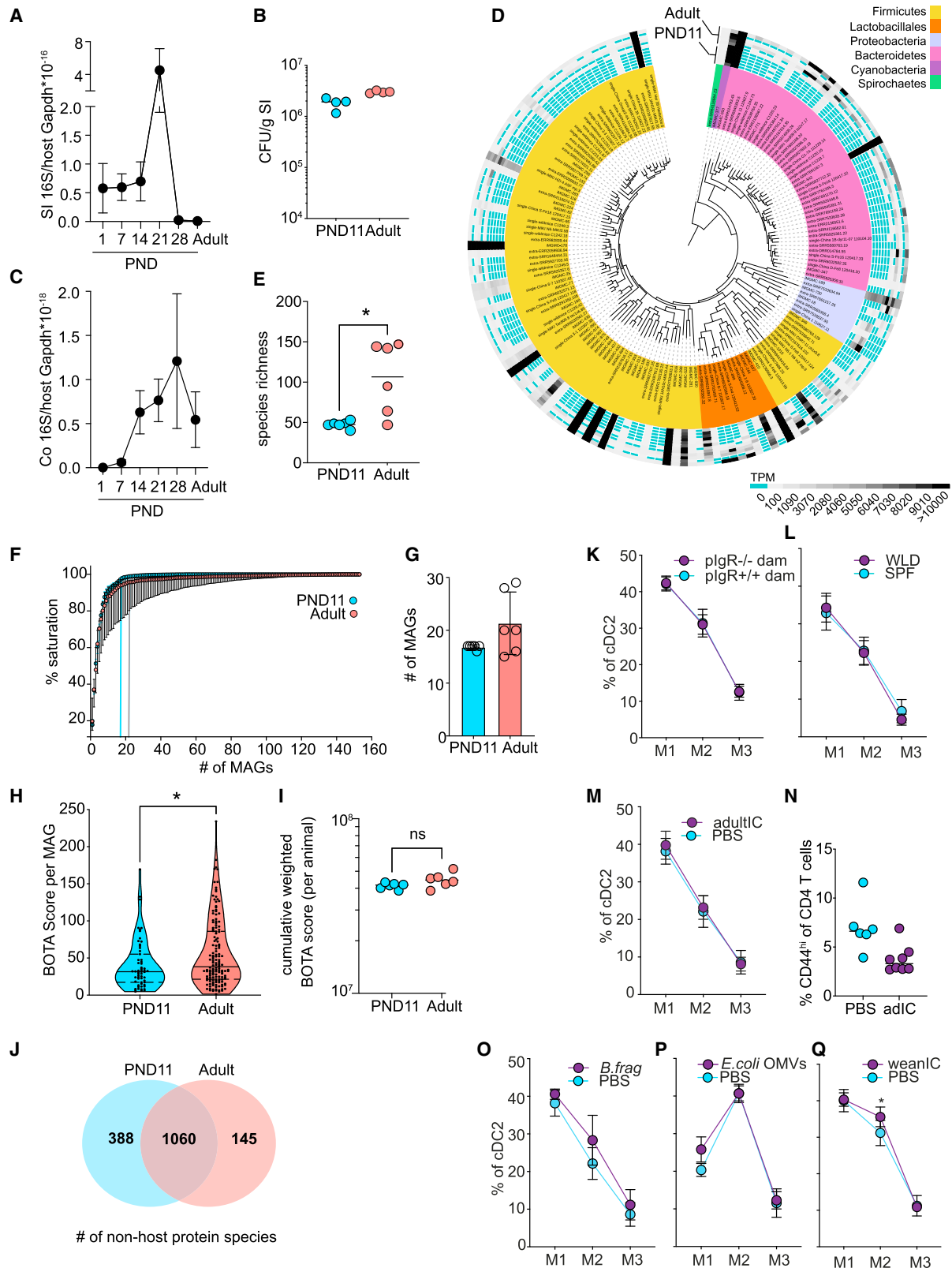
Figure 5. Rapid establishment of a dense and immunogenic small intestinal core microbiome in absence of adaptive immune maturation

(A) Bacterial density determined by quantitative 16S rRNA gene qRCR normalized to murine *Gapdh* in total small intestinal (SI) tissue (n = 5, mean + SD, Kruskall-Wallis/Dunn's multiple comparison to adult).

also enriched at M2 in animals with myeloid-specific MyD88 deficiency (MyD88$^{\Delta CD11c}$), important for microbiota-dependent innate immune signaling (Figure S4D).[33] Taken together our results identify markers of cDC2 maturation and show that microbiota-derived signals promote cDC2 and RORγt$^+$ APC maturation after birth.

Early rise in SI microbiota density, diversity, and antigenicity

Lack of innate immune stimulation or reduced exposure to microbial immunogenic antigens might contribute to the observed delay in MNP maturation. We comparatively analyzed the density and composition of the SI microbiota in neonatal and adult mice by quantitative (q) PCR and metagenomic sequencing, respectively. qPCR for bacterial 16S rRNA gene copies revealed a high bacterial load as early as 24 h post parturition remaining unchanged until PND14 in SI tissue with a further transient increase during weaning but not a reduced bacterial load during early life compared with adult (Figure 5A). Similarly, anaerobic culture of luminal material on nutrient-rich agar plates revealed a comparable number of colony-forming units (CFUs) per gram SI tissue (Figure 5B). Fluorescence *in situ* hybridization (FISH) staining using a eubacterial probe on cross-sections in neonatal (PND11) and adult mice revealed a patchy distribution of commensal bacteria but overall confirmed a similar bacterial load in PND11 and adult mice (Figure S5). A delayed increase in the bacterial density was detected in the colon (Figure 5C). Sequence reads from metagenomic sequencing of DNA prepared from luminal material of neonatal and adult small intestines were matched against the integrated mouse gut metagenome catalog (iMGMC)[34] and 164 metagenome-assembled genomes (MAGs) were identified (Figure 5D; Table S1). The overall species richness was higher in adult than neonatal mice (Figure 5E) but was largely confined to low abundance species. The core microbiome represented by highly abundant MAGs, mostly of the Firmicutes and Bacteroidetes phyla, was present early in life (Figure 5D). By calculating knee points in saturation plots, we could confirm that the number of species to reach saturation was not significantly different between both age groups (Figures 5F and 5G).

Beside the strength of innate immune signals, a reduced spectrum of immunogenic peptides derived from microbiota in the neonatal vs. adult SI might explain the observed delay in immune maturation after birth. Using MAGs identified in neonatal and adult small intestine in combination with a previously reported *in silico* pipeline bacteria-origin T cell antigen (BOTA) predictor to determine peptides likely to be presented on host MHCII molecules derived from proteins encoded in bacterial genomes.[35] Scoring the 164 MAGs revealed a higher mean BOTA score for MAGs present in adult compared with the neonatal consortium (Figure 5H). Consistent with the presence of most highly abundant taxa in the neonate intestine, however, the cumulative weighted BOTA score that incorporates the abundance of detected species showed no significant difference between neonatal (PND11) and adult mice (Figure 5I). Similarly, proteomic analysis of intestinal content reflecting mainly proteins of highly abundant bacterial taxa revealed a large core proteome of 1,060 proteins in both neonatal (PND11) and adult mice and a much smaller number of 388 and 145 age-specific proteins, respectively (Figure 5J; Table S2). Thus, global lack of innate immune stimulation or immunogenic microbial antigens are unlikely factors to explain the delayed MNP maturation in the neonatal host. Instead, specific microbial signals from less abundant taxa might exert an effect.

Next, we analyzed cDC2 maturation (M1–M3) in neonatal mice under various conditions associated with an altered microbiota exposure. Breast milk from pIgR-deficient dams have greatly reduced SIgA-specific for enteric bacteria.[21,36] pIgR$^{+/-}$ offspring from pIgR$^{-/-}$ dams, however, exhibited no detectable difference in PP cDC2 maturation (Figure 5K). Mice with a microbiome like in their natural environment ("wildlings") exhibit a highly diverse microbiota and contain higher numbers of antigen-experienced lymphocytes in the adult.[37–39] Nevertheless, we did not observe differences in subset or stage composition of cDC2 in neonatal PP (data not shown and Figure 5L). To test whether the adult antigenic repertoire would induce T cell priming in the neonate, we gavaged intestinal content from adult animals (adultIC) to neonatal mice. No detectable influence of adult microbiota on PP cDC2 maturation was detected (Figure 5M) and, consistently, the proportion of CD4$^+$ T$_{EM}$ at PND14 was not influenced

(B) Anaerobic culture of homogenized small intestinal tissue (n = 4, mean, Mann-Whitney U test).

(C) Bacterial density determined by quantitative 16S rDNA quantitative real-time PCR normalized to murine *Gapdh* in total colonic tissue (n = 5, mean + SD, Kruskall-Wallis/Dunn's multiple comparison to adult).

(D) Phylogenetic placement, phylum assignment (inner circle), and relative abundance (outer circle) of metagenome-assembled genomes (MAGs) in the SI luminal content by shotgun sequencing.

(E) Molecular species richness determined in (D) (n = 6, mean, Mann-Whitney U test).

(F) Saturation plot depicting number of MAGs required to cover most of the functional potential (n = 6, median + SD). Knee points indicated with vertical lines.

(G) Knee points of the individual saturation curves indicated in (F) (n = 6, mean + SD, Mann-Whitney U test).

(H) BOTA scores of all MAGs from (D) (n$_{PND11}$ = 59, n$_{Adult}$ = 149 MAGs, violin plot, Mann-Whitney U test).

(I) Cumulative abundance-weighted BOTA scores from (D) (n = 6, mean, Mann-Whitney-U test).

(J) Venn diagram of non-host-derived protein species identified by mass spectrometry in small intestinal luminal material (n = 6).

(K and L) Percentage of M1–M3 of cDC2 in PND11 (K) pIgR$^{+/-}$ offspring born to pIgR$^{-/-}$ dams or pIgR$^{+/+}$ offspring born to pIgR$^{+/+}$ dams (n = 4–5) and (L) wildling (WLD) animals (n = 11–12), (mean + SD; two-way ANOVA/Bonferroni test between genetic groups within the same maturational stage) determined by FACS.

(M) Percentage of M1–M3 of cDC2 in PND12 mice after oral administration of adult intestinal content (adultIC) on PND9-11 (n = 5), (mean + SD; two-way ANOVA/Bonferroni test between treatment groups within the same maturational stage).

(N) Percentage of CD44^{hi} cells among total PP CD4$^+$ T cells in 14-day-old mice after oral administration of adult intestinal content (adultIC) on PND1-9 (n = 6–8; median).

(O–Q) Percentage of M1–M3 of cDC2 in PND12 mice that were administered (O) *B. fragilis* by oral gavage on PND9-11 (n = 5), (P) 8 h after *E. coli* OMVs oral gavage (n = 6–7), and (Q) weaning intestinal content (weanIC) by oral gavage on PND9-11 (n = 5–9) (mean + SD, two-way ANOVA/Bonferroni test between treatment groups within the same maturational stage). See also Figure S5 and Tables S1 and S2.

(Figure 5N). *Bacteroides spp.* as well as microbiota-derived outer membrane vesicles (OMVs) exert immune maturation activity.[40,41] Oral application of a murine strain of *Bacteroides fragilis* or OMVs isolated from *E. coli* did not influence PP cDC2 maturation (Figures 5O and 5P). Finally, we gavaged intestinal content from weaning animals (weanIC) to neonatal mice in order to test the PP maturation promoting effect of bacterial taxa that exhibit a transiently enhanced abundance during the shift from a neonatal to an adult microbiota.[42] An enhanced proportion of stage M2 (CD11b$^+$) cDC2 cells was detected upon administration of weanIC (Figure 5Q). Thus, the murine SI is colonized rapidly after birth and global differences in luminal bacterial density, composition and antigenicity appear not to account for the observed delay in DC maturation in the neonatal host. Instead, signals from specific taxa with enhanced abundance during weaning may contribute to PP DC maturation.

IFN I promotes activation of PP DC but does not recapitulate adult to neonatal transition

Endogenous immune stimuli might induce PP DC maturation. IFN-stimulated genes (ISGs) such as *Ifitm1*, *Ifitm2*, and *Ifitm3* showed the greatest expression reduction in neonatal cDC2 but also cDC1 (Figures 1H and 1I). Tonic-microbiota-induced IFN I signaling was shown to enhance antimicrobial resistance in adult animals.[11] Therefore, increased IFN I signaling might also promote maturity and functionality of neonatal PP MNP. To test this hypothesis, we employed the Toll-like receptor (TLR) 7 ligand R848, which activates SI LP and PP DC in adult animals via release of IFN I and TNF-α by plasmacytoid (p)DC.[25,43] Neonatal mice exhibited a higher proportion of PP pDC (Figure S6A) and enhanced expression of the co-stimulatory molecule CD86 at 8h after oral administration of R848 (Figure S6B). Proinflammatory serum cytokines, including IFN I, were higher in neonatal animals compared with their adult counterparts following R848 treatment (Figure 6A). R848 treatment also promoted cDC2 progression to M2 and M3 and enhanced the percentage of CCR7$^+$-activated cDC1 and RORγt$^+$ APC (Figures 6B–6D).

We addressed how oral R848 affected adaptive immune priming and memory formation in neonates. OTII priming in neonatal PP was diminished compared with adult PP (Figure 3B) but oral co-administration of R848 with OVA partially reversed this phenotype (Figures 6E and S6F). Next, the influence of R848 on T and B cell responses was studied using a vaccination protocol with peracetic acid (PAA)-inactivated, orally administered *Salmonella* Typhimurium (STm) followed by oral challenge with viable *S.* Typhimurium in the adult animal as previously described (Figure 6F).[44] R848 administration with the first and second vaccine dose at PND7 and 14, respectively, enhanced the percentage of Th1 cells. However, it diminished the percentage of IFNγ$^+$ CD8 cytotoxic T cells (Figures 6G and S6G). Further, R848 abrogated the anti-STm IgA response in the SI mucosa (Figure S6H). The systemic anti-STm IgG and IgM antibody response showed a similar trend (Figures S6I and S6J).

R848 potently activated neonatal PP APC (Figures 6B–6E). To better understand whether the effect of R848 mimicked the physiological PP APC maturation during the neonatal-to-adult transition, sorted PP phagocytes from PND11 and adult mice orally treated with R848 or PBS were subjected to scRNA-seq

analysis (Figure 6H). Although neonatal mice exhibited a very potent systemic response to R848 (Figure 6A), the local mucosal response was less pronounced than in the adult, as depicted by the changes in qDC/actDC ratios for cDC1 and cDC2 (Figure 6H). Transcriptional changes after R848 administration were mainly driven by elevated ISG expression, with *Isg15*, *Irf7*, *Ifi27l2a*, and *Ifitm3* being among the top 10 increased genes both in adult and neonatal qDC2, qDC1, and RORγt$^+$ APC (Figures 6I and S6C). Pseudotime trajectory analysis of cDC2, cDC1, and RORγt$^+$ APC confirmed an activation pattern of DCs in R848-treated animals. R848-mediated activation was distinct from the homeostatic activation and mainly defined by an enhanced ISG profile with a bimodal splitting of the CCR7$^+$ cells into two different branches representing steady state vs. R848 (Figures 6J, S6D, and S6E). Further, we analyzed genes and corresponding GO terms that were differentially expressed in both, adult vs. neonatal and PND11 PBS vs. R848 comparisons (Figure S7). Very few genes were co-regulated in both datasets. Even within common GO terms, different genes contributed to GO term enrichment, illustrating that the IFN-I-driven activation in the neonate did not recapitulate the neonatal-to-adult transition. Adult mice deficient in the IFN type I receptor in CD11c$^+$ cells (IFNAR$^{\Delta IEC}$) exhibited no decrease in PP cDC2 maturation (Figure 6K). Thus, the type-I-IFN-inducer R848 stimulated a strong systemic cytokine response in neonates and was able to overcome the maturational arrest of neonatal DC in respect to CD4$^+$ T cell priming. However, despite its potent activity, IFN I appear not to represent the physiological stimulus that drives PP APC maturation in steady state.

Appearance of M cells determines post-natal cDC2 maturation

M cells as part of the PP FAE represent the primary site of luminal sampling and translocation of particulate antigen, which initiates mucosal IgA production to commensal enteric bacteria.[45] M cells are absent from the FAE of neonatal mice and appear only during the third week of life as illustrated by the age-dependent expression of the M cell master transcription factor SpiB and markers Ccl9 and Gp2 (Figure 7A) and staining of GP2$^+$ mature M cells in the FAE (Figure 7B).[46,47] The age-dependent appearance of M cells was functionally relevant, illustrated by differences in the uptake of orally administered fluorescent 100-nm latex beads by SED phagocytes between neonatal and adult PP (Figure 7C). Whereas >90% of sections of adult PP contained bead-positive phagocytes in the SED, only approximately 40% of neonatal PP phagocytes had internalized beads at 6 h after oral gavage (Figure 7D). Also, the number of intra-phagocytic beads in the SED was reduced in the neonate (Figure 7E). Thus, the differentiation of M cells and their function as gatekeepers of luminal microbial stimuli might induce PP APC maturation. Indeed, adults lacking M cells due to receptor activator of NF-κB (RANK) deficiency in the intestinal epithelium exhibited impaired maturity of cDC2 in PP tissue (Figure 7F).[48] Inversely, accelerated induction of M cells in PND11 mice through administration of RANK ligand enhanced the fraction of M2 PP cDC2 (Figure 7G). In addition to RANK ligand, the TLR5 ligand flagellin will stimulate M cell development.[49] Consistently, administration of flagellin induced premature appearance of GP2$^+$ M cells (Figure 7J) and enhanced cDC2 maturity
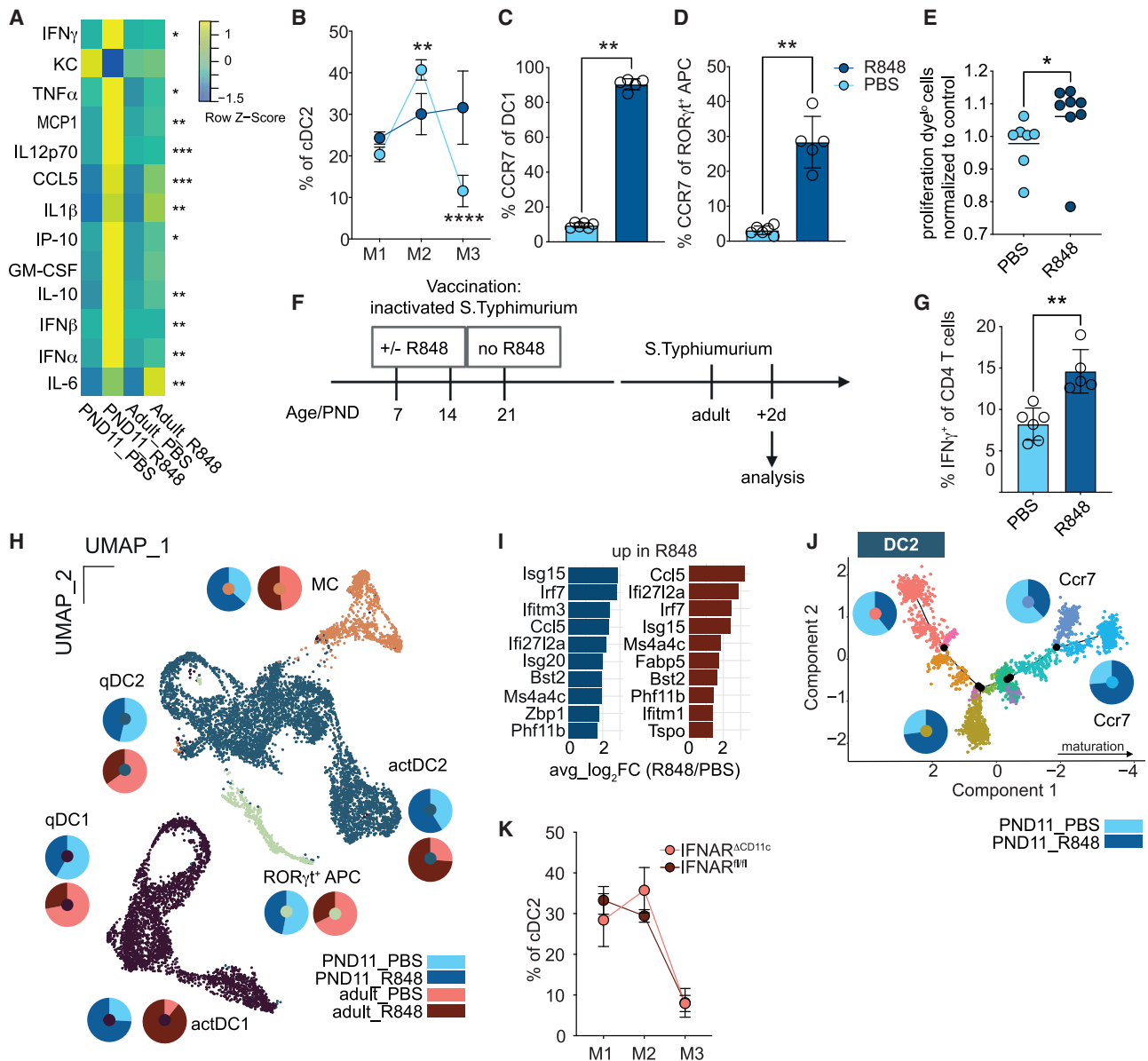
Figure 6. IFN I induces DC activation in neonatal PP and modifies the adaptive immune response

(A) Heatmap of serum cytokines 8 h after R848 (n = 4–5; Kruskall-Wallis test, comparison within age group).

(B) Percentage of M1–M3 of cDC2 in PND11 mice after R848 (n = 4–5), (mean + SD; two-way ANOVA/Bonferroni test between treatment groups within the same maturational stage) determined by FACS.

(C and D) Percentage of CCR7$^+$ among (C) cDC1 and (D) RORγt$^+$ APC in PP after R848 in PND11 mice (mean + SD, Mann-Whitney U test).

(E) Proliferation dye dilution in OTII cells in PP of neonatal mice 48 h after oral gavage of OVA ± R848 normalized to mean PBS (n = 7–8, mean, Mann-Whitney U test).

(F) Neonatal PAA-STm/R848 vaccination experimental setup.

(G) Percentage of IFN$\gamma$$^+$ of CD4$^+$ T cells in colonic LP of STm infected mice vaccinated with PAA STm ± R848 as neonates (n = 5–6, mean + SD, Mann-Whitney U test).

(H) scRNA-seq of PP MNP (n = 1; cells pooled from 4 animals per sample).

(I) Top 10 upregulated genes in PND11 (dark blue) and adult (berry) R848 vs. PBS qDC2.

(J) Pseudotime trajectory of cDC2 from PND11 mice ± R848, pie charts represent the relative contribution of cells from PBS and R848 treated animals to indicated branches.

(K) Percentage of M1–M3 of cDC2 in adult IFNAR$^{\Delta CD11c}$ and IFNAR$^{fl/fl}$ mice (n = 5), (mean + SD, two-way ANOVA and Bonferroni test between genetic groups within the same maturational stage) determined by FACS. See also Figures S6 and S7.
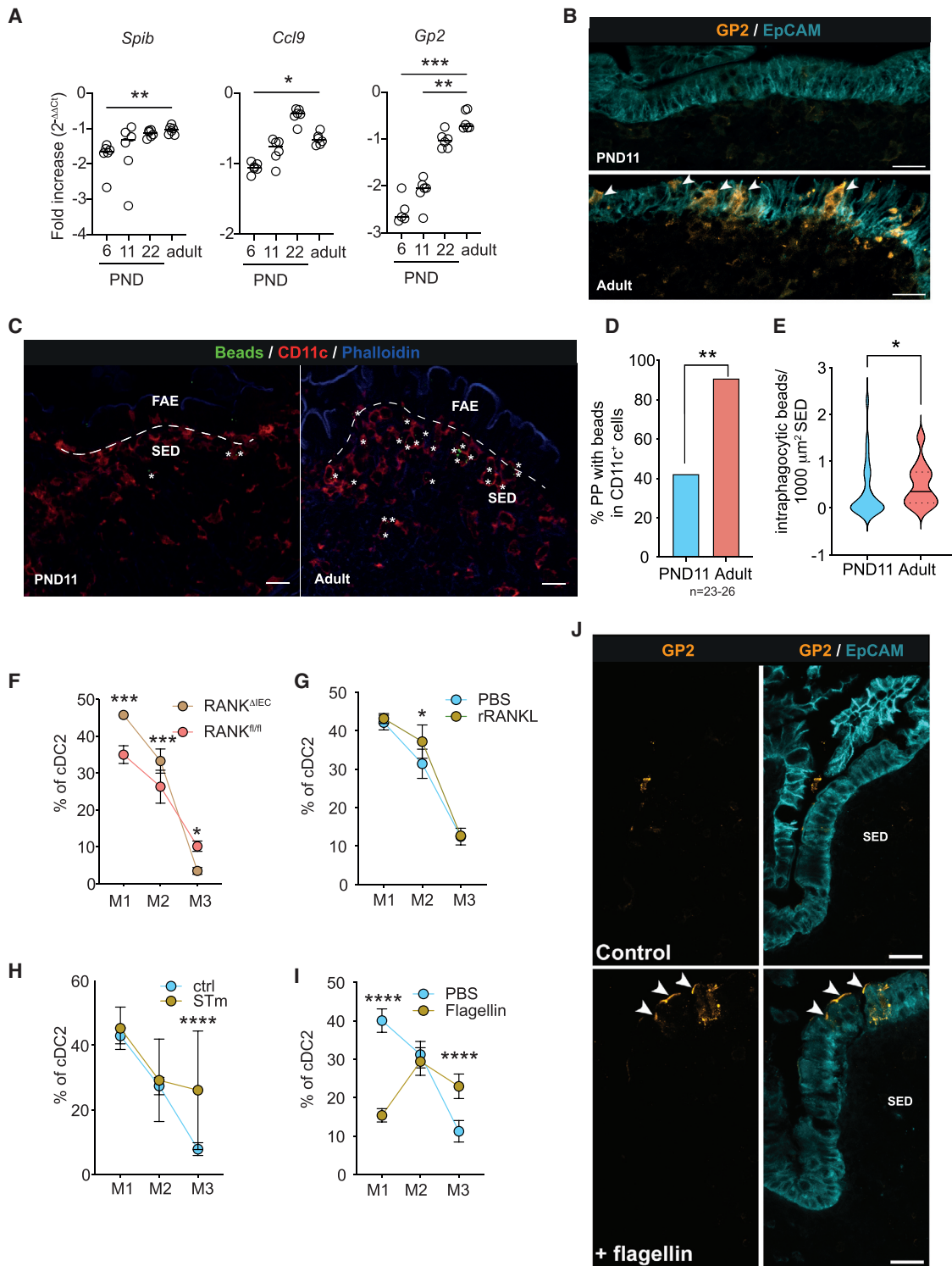
Figure 7. M cells are associated with PP DC maturation

(A) Quantitative real-time PCR of *Spib*, *Ccl9*, and *Gp2* from PP (n = 5–6, mean, Brown, Forsyth, and Welch ANOVA).

(B) Spectral confocal imaging projection representative of PP dome regions. Sections illustrate epithelial cells and M cells (right panels) using EpCAM (cyan) and GP2 (orange). Arrowheads point toward M cells in the FAE. Scale bars, 20 μm.

(C) Immunofluorescence imaging representative of PND11 and adult PP after oral administration of 100-nm fluorescent beads stained for CD11c (red), phalloidin (blue), beads (green); asterisks indicate intraphagocytic beads in the SED. Scale bars, 20 μm.

(D) Percentage of PP with beads in CD11c+ cells within the SED (n = 23–26 follicles from 4 animals, Fisher's exact test).

(Figure 7I). STm induces M cell maturation to facilitate its own uptake.[50,51] Consistently, infection with STm enhanced the percentage of CCR7⁺ mature PP cDC2 (Figure 7H). Together, our results suggest a contribution of FAE M cells to the maturation of PP APC. Beside specific microbial signals provided by the microbiota at weaning, the appearance of M cells during the 3rd week after birth critically influences the emergence of fully mature PP APC that in turn regulate the maturation of mucosal T cells, germinal center B cells and the production of secretory IgA.

DISCUSSION

The ontogeny of immune maturation is of major conceptual and functional relevance. Epidemiological studies highlight the early post-natal period as a critical and non-redundant time window for the establishment of a fully functional mucosal immune system.[4,6,52–57] Also, immune maturation represents a timed succession of events that activate regulatory features prior to effector functions to maintain homeostasis.[24,58] Characterization of the post-natal immune maturation advances our understanding of the mechanisms that facilitate life-long immune homeostasis and determine the susceptibility to inflammatory and immune-mediated diseases.

Our results show that delayed post-natal PP CD4⁺ T cell maturation is paralleled by changes in the APC subset composition, localization, and cell differentiation. Given the principle functionality of neonatal T cells, the underrepresentation and functional impairment of cDC2 function could explain the prolonged low frequency of activated CD4⁺ T cells and germinal center B cells after birth.[59–62] Additional factors might contribute but the previously identified mechanisms namely maternal immunoglobulins and neonatal T regulatory cells, only accounted for a minor part of this suppression.[18,63] In contrast to cDC2, cDC1 were overrepresented, displayed a similar localization and conferred an adult-like activation of transferred OTI cells in the neonatal PP. Also, RORγt⁺ APC were overrepresented in the neonatal PP and their numbers were enhanced by the presence of a viable microbiota in early but not later life. RORγt⁺ ILC3-like APCs have recently been described in the MLN and shown to be required for peripheral regulatory T cells (pTregs) induction.[22,23] However, the transcriptional profile of RORγt⁺ APC clearly clustered with DC rather than ILC3 or natural killer (NK) cells and failed to express important ILC3 marker molecules. Another group recently described antigen-presenting RORγt⁺ TCs in the MLN that emerge during an early time window and also induce pTreg in the colon.[24] PP RORγt⁺ APC displayed an intermediate level of similarity with the CCR7⁺ fraction of MLN TCs but were present at high levels already in the first vs. second week of life and did not express the gene for cleavage of TGF-β, Itgb8, which was shown by Akagbosu et al.[24] to be the mechanism through which

pTregs were induced. Thus, the function of RORγt⁺ APC is likely different from TCs. PP RORγt⁺ APC might still exert tolerogenic function through other, tissue-environment-specific mechanisms or contribute to type III immune responses. Type III immune responses are driven by IL-17, and we detected increased levels of IL-17 in the PP MNP OTII co-cultures from neonatal mice. RORγt⁺ APC have also been detected in the SPL of neonatal mice and thus might represent a more global feature of the neonatal immune system.[27] Also, the ontogeny of neonatal RORγt⁺ APC remains unknown. Their dependency on Clec9a-expressing progenitors was ruled out.[24,27] However, as neonatal cDC2 unlike their adult counterparts also largely do not derive from Clec9a⁺ precursors, it remains to be tested whether RORγt⁺ APC have a common precursor with cDC.[27] Taken together, APC T cell interactions in the neonate are characterized by ignorance of microbiota-derived antigen, a DC1 over DC2 bias, and the presence of RORγt⁺ APC with yet unknown function. APC in the neonatal PP appear to be designated to not engage in homeostatic crosstalk but respond efficiently to pathogenic, mostly viral, challenge in accordance with many previous reports.[60,64]

The high frequency of activated CD4⁺ T cells in the healthy adult intestine reflects the continuous and intense interaction between the mucosal immune system and the enteric microbiota. We found that the SI microbiota exhibits a high bacterial density, substantial microbial diversity and broad antigenicity early after birth, similar to what has been described in the oral cavity.[65] A delayed increase in bacterial diversity over 2–3 years in humans and 6–8 weeks in mice was described, but these studies lacked a quantitative analysis and investigated fecal samples that reflect the distal intestinal tract.[42,66–68] A global lack of innate stimuli or limited spectrum of immunogenic antigens therefore appears an unlikely explanation for the delayed T cell maturation in the murine neonatal small intestine.

Nevertheless, a significant difference in the maturation stage and number of cDC2 and RORγt⁺ APC was observed between SPF and GF animals, respectively. Several attempts failed to identify the underlying stimulus. Only the transfer of a weaning age microbiota exerted a significant stimulatory effect. The subsequent identification of the critical role of M cell development and the differentiation-promoting effect of flagellin hints to a possible role of flagellated taxa with only transient abundance. Flagellated bacterial taxa may bloom during the early post-natal period with loss of the recently discovered TLR 5-mediated counterselection of flagellated bacteria in the small intestine.[69]

Instead, the age-dependent differentiation of M cells within the FAE was required and sufficient to initiate cDC2 maturation. M cells show a characteristic morphology and provide sufficient luminal antigen to supply underlying PP APC through their high endocytotic and transcytotic capacity.[70–72] We found that cDC2 accumulated at and interacted tightly with the neonatal

FAE prior to M cell maturation possibly awaiting antigen delivery. Consistently, expression of the successive M cell maturation markers SipB, Ccl9, and Gp2 increased steadily during postnatal development in our study and previous reports.[46,47,73,74] Receptor activator of nucleic factor-kappa B ligand (RANKL) expressed by subepithelial stromal M cell inducer (MCi) cells stimulates M cell differentiation in adult mice.[75] Since parenteral RANKL administration to neonatal mice induced premature M cell differentiation, the pace of MCi cell differentiation and their ability to present RANKL may ultimately determine the onset of M cell differentiation. Alternatively, inhibitory signals like the developmental regulator Blimp1, suppressive factor ONECUT2 or breast-milk constituents such as epidermal growth factor (EGF) may reduce the sensitivity of the FAE to RANKL or reduce RANKL expression or its signal strength.[76–78] Future work needs to address the influence of developmental and exogenous factors on M cell development.

M cells also serve as scaffold for certain types of APC to directly sample luminal material for subsequent processing and presentation.[71] Interestingly, we observed enhanced numbers of cDC2 that interacted with the neonatal FAE and exhibited membrane extensions toward the FAE surface. These epithelium-associated cDC2 might receive the first luminal material translocated by emerging M cells after weaning.[79] In wildling mice, cDC2 still exhibited a delayed time course of immune maturation suggesting that exposure to viral or bacterial pathobionts or pathogens might not suffice to accelerate M cell differentiation.

A mechanistic understanding of ontogenetic features of immune maturation and their biological relevance as well as the ability to manipulate immune reactivity might ultimately facilitate age-adapted interventional precision strategies to prevent or treat diseases of the term and preterm human neonate.[80] Infections represent the main cause of morbidity and mortality in neonates and young infants worldwide and preventive measures such as vaccines could reduce childhood mortality.[74,81–88] The use of vaccines in neonates that carry the largest disease burden, however, is less effective calling for strategies to accelerate immune maturation and improve the immune response to the vaccine antigen in particular at mucosal body surfaces accessible to non-parenteral vaccine administration.[80]

Limitations of the study

Important questions remain about antigen acquisition by MNPs, both in neonatal and adult PPs. For example, whereas cDC2 reside in both SED and IFR and likely sample antigen directly, IFR-resident cDC1 may rely on antigen transfer from other phagocytes. In contrast, MCs localize next to M cells and take up particulate antigen but migrate and prime T cells inefficiently. Therefore, putative antigen transfer from MCs might be an important mechanism of antigen acquisition that merits further investigation. Likewise, it remains unclear whether PP uptake of soluble and particulate antigens entails different routes.

We identified M cell development as prerequisite for cDC2 maturation; however, cellular and molecular mediators of M cell development largely remain unclear. Finally, we demonstrated selective enrichment of RORgt+ APC in neonatal PPs. Low cell numbers precluded functional ex vivo studies, but future studies utilizing genetic mouse models will address their function in steady state and inflammation.

STAR★METHODS

Detailed methods are provided in the online version of this paper and include the following:

- KEY RESOURCES TABLE
- RESOURCE AVAILABILITY
  - Lead contact
  - Materials availability
  - Data and code availability
- EXPERIMENTAL MODEL AND SUBJECT DETAILS
  - Animals
  - In vivo models
  - Vaccination against *S.*Typhiumrium/ *S.*Typhimurium infection
- METHOD DETAILS
  - Isolation of PP cells
  - Flow cytometry and cell sorting
  - DC OTII co-culture and T helper cytokine induction
  - Quantification of 16S rRNA gene copy numbers
  - Quantification of bacteria by anaerobic culture
  - Immunofluorescence and confocal microscopy
  - Quantification of the CD11c signal distribution in PP
  - Single cell RNA sequencing and analysis
  - Shotgun metagenomic sequencing
  - Metagenomic data analysis
  - Antigenic peptide prediction from metagenomic data using BOTA
  - Metaproteomic analysis
- QUANTIFICATION AND STATISTICAL ANALYSIS

REFERENCES

1. Herzenberg, L.A., and Herzenberg, L.A. (1989). Toward a layered immune system. Cell *59*, 953–954. https://doi.org/10.1016/0092-8674(89)90748-4.

2. Hornef, M.W., and Torow, N. (2020). 'Layered immunity' and the 'neonatal window of opportunity' - timed succession of non-redundant phases to establish mucosal host-microbial homeostasis after birth. Immunology *159*, 15–25. https://doi.org/10.1111/imm.13149.

3. Abdel-Gadir, A., Stephen-Victor, E., Gerber, G.K., Noval Rivas, M., Wang, S., Harb, H., Wang, L., Li, N., Crestani, E., Spielman, S., et al. (2019). Microbiota therapy acts via a regulatory T cell MyD88/RORgammat pathway to suppress food allergy. Nat. Med. *25*, 1164–1174. https://doi.org/10.1038/s41591-019-0461-z.

4. Cahenzli, J., Köller, Y., Wyss, M., Geuking, M.B., and McCoy, K.D. (2013). Intestinal microbial diversity during early-life colonization shapes long-term IgE levels. Cell Host Microbe *14*, 559–570. https://doi.org/10.1016/j.chom.2013.10.004.

5. Lynn, M.A., Tumes, D.J., Choo, J.M., Sribnaia, A., Blake, S.J., Leong, L.E.X., Young, G.P., Marshall, H.S., Wesselingh, S.L., Rogers, G.B., et al. (2018). Early-life antibiotic-driven dysbiosis leads to dysregulated vaccine immune responses in mice. Cell Host Microbe *23*, 653–660.e5. https://doi.org/10.1016/j.chom.2018.04.009.

6. Olszak, T., An, D., Zeissig, S., Vera, M.P., Richter, J., Franke, A., Glickman, J.N., Siebert, R., Baron, R.M., Kasper, D.L., and Blumberg, R.S. (2012). Microbial exposure during early life has persistent effects on natural killer T cell function. Science *336*, 489–493. https://doi.org/10.1126/science.1219328.

7. Zanvit, P., Konkel, J.E., Jiao, X., Kasagi, S., Zhang, D., Wu, R., Chia, C., Ajami, N.J., Smith, D.P., Petrosino, J.F., et al. (2015). Antibiotics in neonatal life increase murine susceptibility to experimental psoriasis. Nat. Commun. *6*, 8424. https://doi.org/10.1038/ncomms9424.

8. Kirjavainen, P.V., Karvonen, A.M., Adams, R.I., Täubel, M., Roponen, M., Tuoresmäki, P., Loss, G., Jayaprakash, B., Depner, M., Ege, M.J., et al. (2019). Farm-like indoor microbiota in non-farm homes protects children

9. Schuijs, M.J., Willart, M.A., Vergote, K., Gras, D., Deswarte, K., Ege, M.J., Madeira, F.B., Beyaert, R., van Loo, G., Bracher, F., et al. (2015). Farm dust and endotoxin protect against allergy through A20 induction in lung epithelial cells. Science *349*, 1106–1110. https://doi.org/10.1126/science.aac6623.

10. Vatanen, T., Kostic, A.D., d'Hennezel, E., Siljander, H., Franzosa, E.A., Yassour, M., Kolde, R., Vlamakis, H., Arthur, T.D., Hämäläinen, A.M., et al. (2016). Variation in microbiome LPS immunogenicity contributes to autoimmunity in humans. Cell *165*, 842–853. https://doi.org/10.1016/j.cell.2016.04.007.

11. Schaupp, L., Muth, S., Rogell, L., Kofoed-Branzk, M., Melchior, F., Lienenklaus, S., Ganal-Vonarburg, S.C., Klein, M., Guendel, F., Hain, T., et al. (2020). Microbiota-induced Type I interferons instruct a poised basal state of dendritic cells. Cell *181*, 1080–1096.e19. https://doi.org/10.1016/j.cell.2020.04.022.

12. Koya, T., Yanagisawa, R., Higuchi, Y., Sano, K., and Shimodaira, S. (2017). Interferon-alpha-inducible dendritic cells matured with OK-432 exhibit TRAIL and Fas ligand pathway-mediated killer activity. Sci. Rep. *7*, 42145. https://doi.org/10.1038/srep42145.

13. Date, I., Koya, T., Sakamoto, T., Togi, M., Kawaguchi, H., Watanabe, A., Kato, T., Jr., and Shimodaira, S. (2020). Interferon-alpha-induced dendritic cells generated with human platelet lysate exhibit elevated antigen presenting ability to cytotoxic T lymphocytes. Vaccines (Basel) *9*, 10. https://doi.org/10.3390/vaccines9010010.

14. Spadaro, F., Lapenta, C., Donati, S., Abalsamo, L., Barnaba, V., Belardelli, F., Santini, S.M., and Ferrantini, M. (2012). IFN-alpha enhances cross-presentation in human dendritic cells by modulating antigen survival, endocytic routing, and processing. Blood *119*, 1407–1417. https://doi.org/10.1182/blood-2011-06-363564.

15. Zietara, N., Łyszkiewicz, M., Gekara, N., Puchałka, J., Dos Santos, V.A., Hunt, C.R., Pandita, T.K., Lienenklaus, S., and Weiss, S. (2009). Absence of IFN-beta impairs antigen presentation capacity of splenic dendritic cells via down-regulation of heat shock protein 70. J. Immunol. *183*, 1099–1109. https://doi.org/10.4049/jimmunol.0803214.

16. Gough, D.J., Messina, N.L., Clarke, C.J., Johnstone, R.W., and Levy, D.E. (2012). Constitutive type I interferon modulates homeostatic balance through tonic signaling. Immunity *36*, 166–174. https://doi.org/10.1016/j.immuni.2012.01.011.

17. Taniguchi, T., and Takaoka, A. (2001). A weak signal for strong responses: interferon-alpha/beta revisited. Nat. Rev. Mol. Cell Biol. *2*, 378–386. https://doi.org/10.1038/35073080.

18. Torow, N., Yu, K., Hassani, K., Freitag, J., Schulz, O., Basic, M., Brennecke, A., Sparwasser, T., Wagner, N., Bleich, A., et al. (2015). Active suppression of intestinal CD4(+)TCRalphabeta(+) T-lymphocyte maturation during the postnatal period. Nat. Commun. *6*, 7725. https://doi.org/10.1038/ncomms8725.

19. Luciani, C., Hager, F.T., Cerovic, V., and Lelouard, H. (2022). Dendritic cell functions in the inductive and effector sites of intestinal immunity. Mucosal Immunol. *15*, 40–50. https://doi.org/10.1038/s41385-021-00448-w.

20. Bunker, J.J., Flynn, T.M., Koval, J.C., Shaw, D.G., Meisel, M., McDonald, B.D., Ishizuka, I.E., Dent, A.L., Wilson, P.C., Jabri, B., et al. (2015). Innate and adaptive humoral responses coat distinct commensal bacteria with immunoglobulin A. Immunity *43*, 541–553. https://doi.org/10.1016/j.immuni.2015.08.007.

21. Pabst, O., and Slack, E. (2020). IgA and the intestinal microbiota: the importance of being specific. Mucosal Immunol. *13*, 12–21. https://doi.org/10.1038/s41385-019-0227-4.

22. Lyu, M., Suzuki, H., Kang, L., Gaspal, F., Zhou, W., Goc, J., Zhou, L., Zhou, J., Zhang, W., et al.; JRI Live Cell Bank (2022). ILC3s select microbiota-specific regulatory T cells to establish tolerance in the gut. Nature *610*, 744–751. https://doi.org/10.1038/s41586-022-05141-x.

23. Kedmi, R., Najar, T.A., Mesa, K.R., Grayson, A., Kroehling, L., Hao, Y., Hao, S., Pokrovskii, M., Xu, M., Talbot, J., et al. (2022). A RORgammat(+) cell instructs gut microbiota-specific Treg cell differentiation. Nature *610*, 737–743. https://doi.org/10.1038/s41586-022-05089-y.

24. Akagbosu, B., Tayyebi, Z., Shibu, G., Paucar Iza, Y.A., Deep, D., Parisotto, Y.F., Fisher, L., Pasolli, H.A., Thevin, V., Elmentaite, R., et al. (2022). Novel antigen presenting cell imparts Treg-dependent tolerance to gut microbiota. Nature *610*, 752–760. https://doi.org/10.1038/s41586-022-05309-5.

25. Bonnardel, J., Da Silva, C., Wagner, C., Bonifay, R., Chasson, L., Masse, M., Pollet, E., Dalod, M., Gorvel, J.P., and Lelouard, H. (2017). Distribution, location, and transcriptional profile of Peyer's patch conventional DC subsets at steady state and under TLR7 ligand stimulation. Mucosal Immunol. *10*, 1412–1430. https://doi.org/10.1038/mi.2017.30.

26. Brown, C.C., Gudjonson, H., Pritykin, Y., Deep, D., Lavallée, V.P., Mendoza, A., Fromme, R., Mazutis, L., Ariyan, C., Leslie, C., et al. (2019). Transcriptional basis of mouse and human dendritic cell heterogeneity. Cell *179*, 846–863.e24. https://doi.org/10.1016/j.cell.2019.09.035.

27. Papaioannou, N.E., Salei, N., Rambichler, S., Ravi, K., Popovic, J., Küntzel, V., Lehmann, C.H.K., Fiancette, R., Salvermoser, J., Gajdasik, D.W., et al. (2021). Environmental signals rather than layered ontogeny imprint the function of type 2 conventional dendritic cells in young and adult mice. Nat. Commun. *12*, 464. https://doi.org/10.1038/s41467-020-20659-2.

28. Cabeza-Cabrerizo, M., Cardoso, A., Minutti, C.M., Pereira da Costa, M., and Reis e Sousa, C. (2021). Dendritic cells revisited. Annu. Rev. Immunol. *39*, 131–166. https://doi.org/10.1146/annurev-immunol-061020-053707.

29. Miller, J.C., Brown, B.D., Shay, T., Gautier, E.L., Jojic, V., Cohain, A., Pandey, G., Leboeuf, M., Elpek, K.G., Helft, J., et al. (2012). Deciphering the transcriptional network of the dendritic cell lineage. Nat. Immunol. *13*, 888–899. https://doi.org/10.1038/ni.2370.

30. Ardouin, L., Luche, H., Chelbi, R., Carpentier, S., Shawket, A., Montanana Sanchis, F., Santa Maria, C., Grenot, P., Alexandre, Y., Gregoire, C., et al. (2016). Broad and largely concordant molecular changes characterize tolerogenic and immunogenic dendritic cell maturation in thymus and periphery. Immunity *45*, 305–318. https://doi.org/10.1016/j.immuni.2016.07.019.

31. Da Silva, C., Wagner, C., Bonnardel, J., Gorvel, J.P., and Lelouard, H. (2017). The Peyer's patch mononuclear phagocyte system at steady state and during infection. Front. Immunol. *8*, 1254. https://doi.org/10.3389/fimmu.2017.01254.

32. Torow, N., and Hornef, M.W. (2017). The neonatal window of opportunity: setting the stage for life-long Host-Microbial Interaction and Immune Homeostasis. J. Immunol. *198*, 557–563. https://doi.org/10.4049/jimmunol.1601253.

33. Hooper, L.V., Littman, D.R., and Macpherson, A.J. (2012). Interactions between the microbiota and the immune system. Science *336*, 1268–1273. https://doi.org/10.1126/science.1223490.

34. Lesker, T.R., Durairaj, A.C., Gálvez, E.J.C., Lagkouvardos, I., Baines, J.F., Clavel, T., Sczyrba, A., McHardy, A.C., and Strowig, T. (2020). An integrated metagenome catalog reveals new insights into the murine gut microbiome. Cell Rep. *30*, 2909–2922.e6. https://doi.org/10.1016/j.celrep.2020.02.036.

35. Graham, D.B., Luo, C., O'Connell, D.J., Lefkovith, A., Brown, E.M., Yassour, M., Varma, M., Abelin, J.G., Conway, K.L., Jasso, G.J., et al. (2018). Antigen discovery and specification of immunodominance hierarchies for MHCII-restricted epitopes. Nat. Med. *24*, 1762–1772. https://doi.org/10.1038/s41591-018-0203-7.

36. Rogier, E.W., Frantz, A.L., Bruno, M.E., Wedlund, L., Cohen, D.A., Stromberg, A.J., and Kaetzel, C.S. (2014). Secretory antibodies in breast milk promote long-term intestinal homeostasis by regulating the gut microbiota and host gene expression. Proc. Natl. Acad. Sci. USA *111*, 3074–3079. https://doi.org/10.1073/pnas.1315792111.

37. Beura, L.K., Hamilton, S.E., Bi, K., Schenkel, J.M., Odumade, O.A., Casey, K.A., Thompson, E.A., Fraser, K.A., Rosato, P.C., Filali-Mouhim, A., et al. (2016). Normalizing the environment recapitulates adult human immune traits in laboratory mice. Nature *532*, 512–516. https://doi.org/10.1038/nature17655.

38. Rosshart, S.P., Herz, J., Vassallo, B.G., Hunter, A., Wall, M.K., Badger, J.H., McCulloch, J.A., Anastasakis, D.G., Sarshad, A.A., Leonardi, I., et al. (2019). Laboratory mice born to wild mice have natural microbiota and model human immune responses. Science *365*, eaaw4361. https://doi.org/10.1126/science.aaw4361.

39. Rosshart, S.P., Vassallo, B.G., Angeletti, D., Hutchinson, D.S., Morgan, A.P., Takeda, K., Hickman, H.D., McCulloch, J.A., Badger, J.H., Ajami, N.J., et al. (2017). Wild mouse gut microbiota promotes Host Fitness and Improves Disease Resistance. Cell *171*, 1015–1028.e13. https://doi.org/10.1016/j.cell.2017.09.016.

40. Stefan, K.L., Kim, M.V., Iwasaki, A., and Kasper, D.L. (2020). Commensal microbiota modulation of natural resistance to virus infection. Cell *183*, 1312–1324.e10. https://doi.org/10.1016/j.cell.2020.10.047.

41. Erttmann, S.F., Swacha, P., Aung, K.M., Brindefalk, B., Jiang, H., Härtlova, A., Uhlin, B.E., Wai, S.N., and Gekara, N.O. (2022). The gut microbiota prime systemic antiviral immunity via the cGAS-STING-IFN-I axis. Immunity *55*, 847–861.e10. https://doi.org/10.1016/j.immuni.2022.04.006.

42. Jiang, H.Q., Bos, N.A., and Cebra, J.J. (2001). Timing, localization, and persistence of colonization by segmented filamentous bacteria in the neonatal mouse gut depend on immune status of mothers and pups. Infect. Immun. *69*, 3611–3617. https://doi.org/10.1128/IAI.69.6.3611-3617.2001.

43. Yrlid, U., Milling, S.W., Miller, J.L., Cartland, S., Jenkins, C.D., and MacPherson, G.G. (2006). Regulation of intestinal dendritic cell migration and activation by plasmacytoid dendritic cells, TNF-alpha and type 1 IFNs after feeding a TLR7/8 ligand. J. Immunol. *176*, 5205–5212. https://doi.org/10.4049/jimmunol.176.9.5205.

44. Moor, K., Wotzka, S.Y., Toska, A., Diard, M., Hapfelmeier, S., and Slack, E. (2016). Peracetic acid treatment generates potent inactivated oral vaccines from a Broad Range of culturable bacterial species. Front. Immunol. *7*, 34. https://doi.org/10.3389/fimmu.2016.00034.

45. Rios, D., Wood, M.B., Li, J., Chassaing, B., Gewirtz, A.T., and Williams, I.R. (2016). Antigen sampling by intestinal M cells is the principal pathway initiating mucosal IgA production to commensal enteric bacteria. Mucosal Immunol. *9*, 907–916. https://doi.org/10.1038/mi.2015.121.

46. Kanaya, T., Hase, K., Takahashi, D., Fukuda, S., Hoshino, K., Sasaki, I., Hemmi, H., Knoop, K.A., Kumar, N., Sato, M., et al. (2012). The Ets transcription factor Spi-B is essential for the differentiation of intestinal microfold cells. Nat. Immunol. *13*, 729–736. https://doi.org/10.1038/ni.2352.

47. Zhang, K., Dupont, A., Torow, N., Gohde, F., Leschner, S., Lienenklaus, S., Weiss, S., Brinkmann, M.M., Kühnel, M., Hensel, M., et al. (2014). Age-dependent enterocyte invasion and microcolony formation by Salmonella. PLoS Pathog. *10*, e1004385. https://doi.org/10.1371/journal.ppat.1004385.

48. Knoop, K.A., Kumar, N., Butler, B.R., Sakthivel, S.K., Taylor, R.T., Nochi, T., Akiba, H., Yagita, H., Kiyono, H., and Williams, I.R. (2009). RANKL is necessary and sufficient to initiate development of antigen-sampling M cells in the intestinal epithelium. J. Immunol. *183*, 5738–5747. https://doi.org/10.4049/jimmunol.0901563.

49. Donaldson, D.S., Pollock, J., Vohra, P., Stevens, M.P., and Mabbott, N.A. (2020). Microbial stimulation reverses the age-related decline in M cells in aged mice. iScience *23*, 101147. https://doi.org/10.1016/j.isci.2020.101147.

50. Tahoun, A., Mahajan, S., Paxton, E., Malterer, G., Donaldson, D.S., Wang, D., Tan, A., Gillespie, T.L., O'Shea, M., Roe, A.J., et al. (2012). Salmonella transforms follicle-associated epithelial cells into M cells to

promote intestinal invasion. Cell Host Microbe *12*, 645–656. https://doi.org/10.1016/j.chom.2012.10.009.

51. Savidge, T.C., Smith, M.W., James, P.S., and Aldred, P. (1991). Salmonella-induced M-cell formation in germ-free mouse Peyer's patch tissue. Am. J. Pathol. *139*, 177–184.

52. Vatanen, T., Kostic, A.D., d'Hennezel, E., Siljander, H., Franzosa, E.A., Yassour, M., Kolde, R., Vlamakis, H., Arthur, T.D., Hämäläinen, A.M., et al. (2016). Variation in microbiome LPS immunogenicity contributes to autoimmunity in humans. Cell *165*, 1551. https://doi.org/10.1016/j.cell.2016.05.056.

53. Ege, M.J., Mayer, M., Normand, A.C., Genuneit, J., Cookson, W.O., Braun-Fahrländer, C., Heederik, D., Piarroux, R., and von Mutius, E.; GABRIELA Transregio 22 Study Group (2011). Exposure to environmental microorganisms and childhood asthma. N. Engl. J. Med. *364*, 701–709. https://doi.org/10.1056/NEJMoa1007302.

54. Depner, M., Taft, D.H., Kirjavainen, P.V., Kalanetra, K.M., Karvonen, A.M., Peschel, S., Schmausser-Hechfellner, E., Roduit, C., Frei, R., Lauener, R., et al. (2020). Maturation of the gut microbiome during the first year of life contributes to the protective farm effect on childhood asthma. Nat. Med. *26*, 1766–1775. https://doi.org/10.1038/s41591-020-1095-x.

55. Constantinides, M.G., Link, V.M., Tamoutounour, S., Wong, A.C., Perez-Chaparro, P.J., Han, S.J., Chen, Y.E., Li, K., Farhat, S., Weckel, A., et al. (2019). MAIT cells are imprinted by the microbiota in early life and promote tissue repair. Science *366*, eaax6624. https://doi.org/10.1126/science.aax6624.

56. Ozkul, C., Ruiz, V.E., Battaglia, T., Xu, J., Roubaud-Baudron, C., Cadwell, K., Perez-Perez, G.I., and Blaser, M.J. (2020). A single early-in-life antibiotic course increases susceptibility to DSS-induced colitis. Genome Med. *12*, 65. https://doi.org/10.1186/s13073-020-00764-z.

57. Martínez, I., Maldonado-Gomez, M.X., Gomes-Neto, J.C., Kittana, H., Ding, H., Schmaltz, R., Joglekar, P., Cardona, R.J., Marsteller, N.L., Kembel, S.W., et al. (2018). Experimental evaluation of the importance of colonization history in early-life gut microbiota assembly. eLife *7*, e36521. https://doi.org/10.7554/eLife.36521.

58. Al Nabhani, Z., Dulauroy, S., Marques, R., Cousu, C., Al Bounny, S., Déjardin, F., Sparwasser, T., Bérard, M., Cerf-Bensussan, N., and Eberl, G. (2019). A weaning reaction to microbiota is required for resistance to immunopathologies in the adult. Immunity *50*, 1276–1288.e5. https://doi.org/10.1016/j.immuni.2019.02.014.

59. Thapa, P., Guyer, R.S., Yang, A.Y., Parks, C.A., Brusko, T.M., Brusko, M., Connors, T.J., and Farber, D.L. (2021). Infant T cells are developmentally adapted for robust lung immune responses through enhanced T cell receptor signaling. Sci. Immunol. *6*, eabj0789. https://doi.org/10.1126/sciimmunol.abj0789.

60. Sarzotti, M., Robbins, D.S., and Hoffman, P.M. (1996). Induction of protective CTL responses in newborn mice by a murine retrovirus. Science *271*, 1726–1728. https://doi.org/10.1126/science.271.5256.1726.

61. Garcia, A.M., Fadel, S.A., Cao, S., and Sarzotti, M. (2000). T cell immunity in neonates. Immunol. Res. *22*, 177–190. https://doi.org/10.1385/IR:22:2-3:177.

62. Forsthuber, T., Yip, H.C., and Lehmann, P.V. (1996). Induction of TH1 and TH2 immunity in neonatal mice. Science *271*, 1728–1730. https://doi.org/10.1126/science.271.5256.1728.

63. Koch, M.A., Reiner, G.L., Lugo, K.A., Kreuk, L.S., Stanbery, A.G., Ansaldo, E., Seher, T.D., Ludington, W.B., and Barton, G.M. (2016). Maternal IgG and IgA antibodies dampen mucosal T helper cell responses in early life. Cell *165*, 827–841. https://doi.org/10.1016/j.cell.2016.04.055.

64. Pott, J., Stockinger, S., Torow, N., Smoczek, A., Lindner, C., McInerney, G., Bäckhed, F., Baumann, U., Pabst, O., Bleich, A., and Hornef, M.W. (2012). Age-dependent TLR3 expression of the intestinal epithelium contributes to rotavirus susceptibility. PLoS Pathog. *8*, e1002670. https://doi.org/10.1371/journal.ppat.1002670.

65. Koren, N., Zubeidat, K., Saba, Y., Horev, Y., Barel, O., Wilharm, A., Heyman, O., Wald, S., Eli-Berchoer, L., Shapiro, H., et al. (2021). Maturation of the neonatal oral mucosa involves unique epithelium-microbiota interactions. Cell Host Microbe *29*, 197–209.e5. https://doi.org/10.1016/j.chom.2020.12.006.

66. Roswall, J., Olsson, L.M., Kovatcheva-Datchary, P., Nilsson, S., Tremaroli, V., Simon, M.C., Kiilerich, P., Akrami, R., Krämer, M., Uhlén, M., et al. (2021). Developmental trajectory of the healthy human gut microbiota during the first 5 years of life. Cell Host Microbe *29*, 765–776.e3. e763. https://doi.org/10.1016/j.chom.2021.02.021.

67. van Best, N., Rolle-Kampczyk, U., Schaap, F.G., Basic, M., Olde Damink, S.W.M., Bleich, A., Savelkoul, P.H.M., von Bergen, M., Penders, J., and Hornef, M.W. (2020). Bile acids drive the newborn's gut microbiota maturation. Nat. Commun. *11*, 3692. https://doi.org/10.1038/s41467-020-17183-8.

68. Yatsunenko, T., Rey, F.E., Manary, M.J., Trehan, I., Dominguez-Bello, M.G., Contreras, M., Magris, M., Hidalgo, G., Baldassano, R.N., Anokhin, A.P., et al. (2012). Human gut microbiome viewed across age and geography. Nature *486*, 222–227. https://doi.org/10.1038/nature11053.

69. Fulde, M., Sommer, F., Chassaing, B., van Vorst, K., Dupont, A., Hensel, M., Basic, M., Klopfleisch, R., Rosenstiel, P., Bleich, A., et al. (2018). Neonatal selection by toll-like receptor 5 influences long-term gut microbiota composition. Nature *560*, 489–493. https://doi.org/10.1038/s41586-018-0395-5.

70. Ohno, H. (2016). Intestinal M cells. J. Biochem. *159*, 151–160. https://doi.org/10.1093/jb/mvv121.

71. Lelouard, H., Fallet, M., de Bovis, B., Méresse, S., and Gorvel, J.P. (2012). Peyer's patch dendritic cells sample antigens by extending dendrites through M cell-specific transcellular pores. Gastroenterology *142*, 592–601.e3. https://doi.org/10.1053/j.gastro.2011.11.039.

72. de Lau, W., Kujala, P., Schneeberger, K., Middendorp, S., Li, V.S., Barker, N., Martens, A., Hofhuis, F., DeKoter, R.P., Peters, P.J., et al. (2012). Peyer's patch M cells derived from Lgr5(+) stem cells require SpiB and are induced by RankL in cultured "miniguts". Mol. Cell. Biol. *32*, 3639–3647. https://doi.org/10.1128/MCB.00434-12.

73. Creamer, B. (1967). The turnover of the epithelium of the small intestine. Br. Med. Bull. *23*, 226–230. https://doi.org/10.1093/oxfordjournals.bmb.a070561.

74. Kotloff, K.L., Nataro, J.P., Blackwelder, W.C., Nasrin, D., Farag, T.H., Panchalingam, S., Wu, Y., Sow, S.O., Sur, D., Breiman, R.F., et al. (2013). Burden and aetiology of diarrhoeal disease in infants and young children in developing countries (the Global Enteric Multicenter Study, GEMS): a prospective, case-control study. Lancet *382*, 209–222. https://doi.org/10.1016/S0140-6736(13)60844-2.

75. Haber, A.L., Biton, M., Rogel, N., Herbst, R.H., Shekhar, K., Smillie, C., Burgin, G., Delorey, T.M., Howitt, M.R., Katz, Y., et al. (2017). A single-cell survey of the small intestinal epithelium. Nature *551*, 333–339. https://doi.org/10.1038/nature24489.

76. Muncan, V., Heijmans, J., Krasinski, S.D., Büller, N.V., Wildenberg, M.E., Meisner, S., Radonjic, M., Stapleton, K.A., Lamers, W.H., Biemond, I., et al. (2011). Blimp1 regulates the transition of neonatal to adult intestinal epithelium. Nat. Commun. *2*, 452. https://doi.org/10.1038/ncomms1463.

77. Knoop, K.A., Gustafsson, J.K., McDonald, K.G., Kulkarni, D.H., Coughlin, P.E., McCrate, S., Kim, D., Hsieh, C.S., Hogan, S.P., Elson, C.O., et al. (2017). Microbial antigen encounter during a preweaning interval is critical for tolerance to gut bacteria. Sci. Immunol. *2*, eaao1314. https://doi.org/10.1126/sciimmunol.aao1314.

78. Luna Velez, M.V.N., H.K., Snabel, R.R., Quint, Y., Qian, C., Martens, A., Veenstra, G.J.C., Freeman, M.R., van Heeringen, S.J., and Vermeulen, M. (2023). ONECUT2 restricts microfold cell numbers in the small intestine; a multi-omics study. https://doi.org/10.1101/2022.09.01.506202.

79. Rivera, C.A., Randrian, V., Richer, W., Gerber-Ferder, Y., Delgado, M.G., Chikina, A.S., Frede, A., Sorini, C., Maurin, M., Kammoun-Chaari, H., et al. (2022). Epithelial colonization by gut dendritic cells promotes their

functional diversification. Immunity *55*, 129–144.e8. https://doi.org/10.1016/j.immuni.2021.11.008.

80. Kollmann, T.R., Marchant, A., and Way, S.S. (2020). Vaccination strategies to enhance immunity in neonates. Science *368*, 612–615. https://doi.org/10.1126/science.aaz9447.

81. G. B. D. Child Mortality Collaborators (2016). Global, regional, national, and selected subnational levels of stillbirths, neonatal, infant, and under-5 mortality, 1980-2015: a systematic analysis for the Global Burden of Disease Study 2015. Lancet *388*, 1725–1774. https://doi.org/10.1016/S0140-6736(16)31575-6.

82. Levine, M.M., Nasrin, D., Acácio, S., Bassat, Q., Powell, H., Tennant, S.M., Sow, S.O., Sur, D., Zaidi, A.K.M., Faruque, A.S.G., et al. (2020). Diarrhoeal disease and subsequent risk of death in infants and children residing in low-income and middle-income countries: analysis of the GEMS case-control study and 12-month GEMS-1A follow-on study. Lancet Glob. Health *8*, e204–e214. https://doi.org/10.1016/S2214-109X(19)30541-8.

83. Mathers, C., Stevens, G., Hogan, D., Mahanani, W.R., and Ho, J. (2017). Global and regional causes of death: patterns and trends. In Disease Control Priorities: Improving Health and Reducing Poverty, RD, D.T. Jamison, H. Gelband, S. Horton, P. Jha, R. Laxminarayan, C.N. Mock, and R. Nugent, eds. (The International Bank for Reconstruction and Development/The World Bank), pp. 2000–2015. https://doi.org/10.1596/978-1-4648-0527-1_ch4.

84. Oppong, T.B., Yang, H., Amponsem-Boateng, C., Kyere, E.K.D., Abdulai, T., Duan, G., and Opolot, G. (2020). Enteric pathogens associated with gastroenteritis among children under 5 years in sub-Saharan Africa: a systematic review and meta-analysis. Epidemiol. Infect. *148*, e64. https://doi.org/10.1017/S0950268820000618.

85. Prudden, H.J., Hasso-Agopsowicz, M., Black, R.E., Troeger, C., Reiner, R.C., Breiman, R.F., Jit, M., Kang, G., Lamberti, L., Lanata, C.F., et al. (2020). Meeting Report: WHO Workshop on modelling global mortality and aetiology estimates of enteric pathogens in children under five. Cape Town, 28-29th November 2018. Vaccine *38*, 4792–4800. https://doi.org/10.1016/j.vaccine.2020.01.054.

86. Costello, A., and Naimy, Z. (2019). Maternal, newborn, child and adolescent health: challenges for the next decade. Int. Health *11*, 349–352. https://doi.org/10.1093/inthealth/ihz051.

87. Boerma, T., Requejo, J., Victora, C.G., Amouzou, A., George, A., Agyepong, I., Barroso, C., Barros, A.J.D., Bhutta, Z.A., Black, R.E., et al. (2018). Countdown to 2030: tracking progress towards universal coverage for reproductive, maternal, newborn, and child health. Lancet *391*, 1538–1548. https://doi.org/10.1016/S0140-6736(18)30104-1.

88. MacLennan, C.A., and Saul, A. (2014). Vaccines against poverty. Proc. Natl. Acad. Sci. USA *111*, 12307–12312. https://doi.org/10.1073/pnas.1400473111.

89. Barnden, M.J., Allison, J., Heath, W.R., and Carbone, F.R. (1998). Defective TCR expression in transgenic mice constructed using cDNA-based alpha- and beta-chain genes under the control of heterologous regulatory elements. Immunol. Cell Biol. *76*, 34–40. https://doi.org/10.1046/j.1440-1711.1998.00709.x.

90. Hogquist, K.A., Jameson, S.C., Heath, W.R., Howard, J.L., Bevan, M.J., and Carbone, F.R. (1994). T cell receptor antagonist peptides induce positive selection. Cell *76*, 17–27. https://doi.org/10.1016/0092-8674(94)90169-4.

91. Caton, M.L., Smith-Raska, M.R., and Reizis, B. (2007). Notch-RBP-J signaling controls the homeostasis of CD8- dendritic cells in the spleen. J. Exp. Med. *204*, 1653–1664. https://doi.org/10.1084/jem.20062648.

92. Hou, B., Reizis, B., and DeFranco, A.L. (2008). Toll-like receptors activate innate and adaptive immunity by using dendritic cell-intrinsic and -extrinsic mechanisms. Immunity *29*, 272–282. https://doi.org/10.1016/j.immuni.2008.05.016.

93. Shen, F.W., Saga, Y., Litman, G., Freeman, G., Tung, J.S., Cantor, H., and Boyse, E.A. (1985). Cloning of Ly-5 cDNA. Proc. Natl. Acad. Sci. USA *82*, 7360–7363. https://doi.org/10.1073/pnas.82.21.7360.

94. Shimada, S., Kawaguchi-Miyashita, M., Kushiro, A., Sato, T., Nanno, M., Sako, T., Matsuoka, Y., Sudo, K., Tagawa, Y., Iwakura, Y., et al. (1999). Generation of polymeric immunoglobulin receptor-deficient mouse with marked reduction of secretory IgA. J. Immunol. *163*, 5367–5373.

95. Kamphuis, E., Junt, T., Waibler, Z., Forster, R., and Kalinke, U. (2006). Type I interferons directly regulate lymphocyte recirculation and cause transient blood lymphopenia. Blood *108*, 3253–3261. https://doi.org/10.1182/blood-2006-06-027599.

96. Jung, S., Aliberti, J., Graemmel, P., Sunshine, M.J., Kreutzberg, G.W., Sher, A., and Littman, D.R. (2000). Analysis of fractalkine receptor CX(3)CR1 function by targeted deletion and green fluorescent protein reporter gene insertion. Mol. Cell. Biol. *20*, 4106–4114. https://doi.org/10.1128/MCB.20.11.4106-4114.2000.

97. Klindworth, A., Pruesse, E., Schweer, T., Peplies, J., Quast, C., Horn, M., and Glöckner, F.O. (2013). Evaluation of general 16S ribosomal RNA gene PCR primers for classical and next-generation sequencing-based diversity studies. Nucleic Acids Res. *41*, e1. https://doi.org/10.1093/nar/gks808.

98. Satija, R., Farrell, J.A., Gennert, D., Schier, A.F., and Regev, A. (2015). Spatial reconstruction of single-cell gene expression data. Nat. Biotechnol. *33*, 495–502. https://doi.org/10.1038/nbt.3192.

99. Trapnell, C., Cacchiarelli, D., Grimsby, J., Pokharel, P., Li, S., Morse, M., Lennon, N.J., Livak, K.J., Mikkelsen, T.S., and Rinn, J.L. (2014). The dynamics and regulators of cell fate decisions are revealed by pseudotemporal ordering of single cells. Nat. Biotechnol. *32*, 381–386. https://doi.org/10.1038/nbt.2859.

100. Li, D., Liu, C.M., Luo, R., Sadakane, K., and Lam, T.W. (2015). MEGAHIT: an ultra-fast single-node solution for large and complex metagenomics assembly via succinct de Bruijn graph. Bioinformatics *31*, 1674–1676. https://doi.org/10.1093/bioinformatics/btv033.

101. Seemann, T. (2014). Prokka: rapid prokaryotic genome annotation. Bioinformatics *30*, 2068–2069. https://doi.org/10.1093/bioinformatics/btu153.

102. Aramaki, T., Blanc-Mathieu, R., Endo, H., Ohkubo, K., Kanehisa, M., Goto, S., and Ogata, H. (2020). KofamKOALA: KEGG ortholog assignment based on profile HMM and adaptive score threshold. Bioinformatics *36*, 2251–2252. https://doi.org/10.1093/bioinformatics/btz859.

103. Bolger, A.M., Lohse, M., and Usadel, B. (2014). Trimmomatic: a flexible trimmer for Illumina sequence data. Bioinformatics *30*, 2114–2120. https://doi.org/10.1093/bioinformatics/btu170.

104. Bushnell, B. (2014). BBMap: A fast, accurate, splice-aware aligner. 9th Annual Genomics of Energy & Environment Meeting.

105. Letunic, I., and Bork, P. (2019). Interactive Tree Of Life (iTOL) v4: recent updates and new developments. Nucleic Acids Res. *47*, W256–W259. https://doi.org/10.1093/nar/gkz239.

106. Salonen, A., Nikkilä, J., Jalanka-Tuovinen, J., Immonen, O., Rajilić-Stojanović, M., Kekkonen, R.A., Palva, A., and de Vos, W.M. (2010). Comparative analysis of fecal DNA extraction methods with phylogenetic microarray: effective recovery of bacterial and archaeal DNA using mechanical cell lysis. J. Microbiol. Methods *81*, 127–134. https://doi.org/10.1016/j.mimet.2010.02.007.

107. Lelouard, H., Mailfert, S., and Fallet, M. (2018). A ten-color spectral imagingstrategy to reveal localization of gut immune cell subsets. https://www.zeiss.fr/content/dam/Microscopy/fr/download/note_application_a_ten_color.pdf.

108. Butler, A., Hoffman, P., Smibert, P., Papalexi, E., and Satija, R. (2018). Integrating single-cell transcriptomic data across different conditions, technologies, and species. Nat. Biotechnol. *36*, 411–420. https://doi.org/10.1038/nbt.4096.

109. Supek, F., Bošnjak, M., Škunca, N., and Šmuc, T. (2011). REVIGO summarizes and visualizes long lists of gene ontology terms. PLoS One *6*, e21800. https://doi.org/10.1371/journal.pone.0021800.

110. Wang, J., Lareau, C.A., Bautista, J.L., Gupta, A.R., Sandor, K., Germino, J., Yin, Y., Arvedson, M.P., Reeder, G.C., Cramer, N.T., et al. (2021). Single-cell multiomics defines tolerogenic extrathymic Aire-expressing populations with unique homology to thymic epithelium. Sci. Immunol. *6*, eabl5053. https://doi.org/10.1126/sciimmunol.abl5053.

111. Godon, J.J., Zumstein, E., Dabert, P., Habouzit, F., and Moletta, R. (1997). Molecular microbial diversity of an anaerobic digestor as determined by small-subunit rDNA sequence analysis. Appl. Environ. Microbiol. *63*, 2802–2813. https://doi.org/10.1128/aem.63.7.2802-2813.1997.

112. Satopaa, V.A., Albrecht, J., Irwin, D., and Raghavan, B. (2011). Finding a "Kneedle" in a Haystack: detecting knee points in system behavior. 2011 31st International Conference on Distributed Computing Systems.

113. Asnicar, F., Thomas, A.M., Beghini, F., Mengoni, C., Manara, S., Manghi, P., Zhu, Q., Bolzan, M., Cumbo, F., May, U., et al. (2020). Precise phylogenetic analysis of microbial isolates and genomes from metagenomes using PhyloPhlAn 3.0. Nat. Commun. *11*, 2500. https://doi.org/10.1038/s41467-020-16366-7.

STAR★METHODS

KEY RESOURCES TABLE

REAGENT or RESOURCE	SOURCE	IDENTIFIER
Antibodies		
CD317 (BSTII) APC (clone 927)	BioLegend	Cat# 127016; RRID:AB_1967127
CD317 (BSTII) BV421 (clone 927)	BioLegend	Cat# 127023; RRID:AB_2687109
CCR7 PE (clone 4B12)	BioLegend	Cat# 120106; RRID:AB_389358
CCR7 PECy5 (clone 4B12)	BioLegend	Cat# 120113; RRID:AB_493571
CD11b BV786 (clone M1/70)	BioLegend	Cat# 101243; RRID:AB_2561373
CD11c PE Cy7(clone N418)	BioLegend	Cat# 117318; RRID:AB_493568
CD11c BUV737 (clone N418)	BD Biosciences	Cat# 749039; RRID:AB_2873433
CD45 APC-R700 (clone 30-F11)	BD Biosciences	Cat# 565478; RRID:AB_2739257
CD45 R718 (clone 30-F11)	BD Biosciences	Cat# 567075
CD64 PE Dazzle 594 (clone X54-5/7.1)	BioLegend	Cat# 139319; RRID:AB_2566558
CD172a (SIRPa) APC (clone P84)	BioLegend	Cat# 144014; RRID:AB_2564061
CD172a (SIRPa) FITC (clone P84)	BioLegend	Cat# 144006; RRID:AB_11204425
I-A/I-E (MHCII) BV510 (clone M5/114.15.2)	BioLegend	Cat# 107635; RRID:AB_2561397
RORgt PE (clone B2D)	Thermo Fisher Scientific	Cat# 12-6981-82; RRID:AB_10807092
XCR1 BV650 (clone ZET)	BioLegend	Cat# 148220; RRID:AB_2566410
XCR1 BV421 (clone ZET)	BioLegend	Cat# 148216; RRID:AB_2565230
CD74 APC (clone In1/CD74)	BioLegend	Cat# 151003; RRID:AB_2632608
CD86 APC (clone GL-1)	BioLegend	Cat# 105011; RRID:AB_493343
IgA PE (clone mA-6E1)	Thermo Fisher Scientific	Cat# 12-4204-81; RRID:AB_465916
IgG1 FITC (clone RG11/39.4)	BD Biosciences	Cat# 553892; RRID:AB_395120
CD4 BV510 (clone RM4-5)	BioLegend	Cat# 100559; RRID:AB_2562608
CD8a BV711 (clone 53-6.7)	BioLegend	Cat# 100748; RRID:AB_2562100
CD44 BV785 (clone IM7)	BioLegend	Cat# 103059; RRID:AB_2571953
CD45.1 BUV 737 (clone A20)	BD Biosciences	Cat# 612811; RRID:AB_2870136
CD45.1 FITC (clone A20)	BioLegend	Cat# 110706; RRID:AB_313495
CD45.2 AF700 (clone 104)	BioLegend	Cat# 109822; RRID:AB_493731
CD69 PE Cy7 (clone H1.2F3)	BioLegend	Cat# 104512; RRID:AB_493564
Va2 BV421 (clone B20.1)	BD Biosciences	Cat# 562944; RRID:AB_2737910
TCRb APC Cy7 (clone H57-597)	BioLegend	Cat# 109220; RRID:AB_893624
GL7 PerCP-Cy5.5 (clone GL7)	BioLegend	Cat# 144609; RRID:AB_2562978
B220 (CD45R) PE/Fire 700 (clone RA3-6B2)	BioLegend	Cat# 103279; RRID:AB_2876408
CD19 Spark NIR 685 (clone 6D5)	BioLegend	Cat# 115568; RRID:AB_2819829
CD3 APC/Fire 810 (clone 17A2)	BioLegend	Cat# 100267; RRID:AB_2876392
IgM eF450 (clone II/41)	Thermo Fisher Scientific	Cat# 48-5790-80; RRID:AB_2574072
IgD BV480 (clone 11-26c.2a)	BD Biosciences	Cat# 566199; RRID:AB_2739590
CD64 (FcγRI) BV605 (clone X54-5/7.1)	BioLegend	Cat# 139323; RRID:AB_2629778
CD45 BUV 395 (clone 30-F11)	BD Biosciences	Cat# 564279; RRID:AB_2651134
CD95 BUV 563 (clone Jo2)	BD OptiBuild	Cat# 741292; RRID:AB_2870823
Chicken anti-GFP unlabeled	Aves Labs	Cat# GFP-1020; RRID:AB_2307313
Hamster anti-mouse CD11c unlabeled (clone N418)	Biolegend	Cat# 117302; RRID:AB_313771
Rabbit anti-mouse IRF8 unlabeled	Bethyl Laboratories	Cat#A304-028A-T; RRID:AB_2620376
Rabbit anti-lysozyme unlabeled	Agilent	Cat# A0099; RRID:AB_2341230
Rat anti-mouse TLR3 unlabeled (clone 11F8)	Bio-Rad	Cat#MCA5891GA
Rat anti-mouse SIRPa unlabeled (clone P84)	Biolegend	Cat# 144002; RRID:AB_11203711

(Continued on next page)

Continued

REAGENT or RESOURCE	SOURCE	IDENTIFIER
Rat anti-ROR gamma (t) unlabeled (clone AFKJS-9)	Thermo Fisher Scientific	Cat# 14-6988-82; RRID:AB_1834475
Rat anti-mouse GP2 unlabeled (clone 2F11-C3)	MBL International	Cat# D278-3; RRID:AB_10598188
Rat anti-mouse CD45 unlabeled (clone 30F11)	Biolegend	Cat# 103101; RRID:AB_312966
Rat anti-mouse CD4-eFluor 450 (clone RM4-5)	Thermo Fisher Scientific	Cat# 48-0042-82; RRID:AB_1272194
Rat anti-mouse Ep-CAM-Alexa Fluor 647 (clone G8.8)	Biolegend	Cat# 118211; RRID:AB_1134104
Donkey anti-chicken IgG- Alexa Fluor 488	Jackson ImmunoResearch	Cat# 703-545-155; RRID:AB_2340375
Donkey anti-rat IgG-Cy3	Jackson ImmunoResearch	Cat# 712-165-153; RRID:AB_2340667
Goat anti-Armenian hamster IgG-Alexa Fluor 594	Jackson ImmunoResearch	Cat# 127-585-160; RRID:AB_2338999
Goat anti-rabbit IgG- Alexa Fluor 514	Thermo Fisher Scientific	Cat# A-31558; RRID:AB_2536173
Bacterial and virus strains		
Bacteroides fragilis	Clavel Lab	CLA-KB-H83 and CLA-JM-H48
Salmonella Typhiumurium	N/A	SL1344
Biological samples		
E.coli OMVs	Gerkara Lab, Erttmann et al.[41]	N/A
PAA *Salmonella* Typhiumurium	Moor et al.[44]	N/A
Chemicals, peptides, and recombinant proteins		
R848	Invivogen	TLRL-R848
Ovalbumin	Sigma	A5253-500G
Ultrapure flagellin from S. typhimurium	Invivogen	tlrl-epstfla-5
RANKL	Biomol	RP0437M-100
Fluoresbrite® YG Microspheres 0.10μm	Polysciences	17150-10
Liberase TH	Sigma Aldrich	5401135001
DNAse I	Sigma Aldrich	11284932001
Critical commercial assays		
LEGENDplex™ Mouse Anti-Virus Response Panel (13-plex) with V-bottom Plate	Biolegend	740622
LEGENDplex™ MU Th Cytokine Panel (12-plex) w/ VbP V03	Biolegend	741044
Chromium Single Cell 3' v2 kit	10xGenomics	PN-120267
Deposited data		
scRNAseq data	this manusript	GSE188714
Metagenomic data	this manusript	BioProject # PRJNA794356
Experimental models: Organisms/strains		
C57BL/6J (B6)	N/A	The Jackson Laboratory
B6.Cg-Tg(TcraTcrb)425Cbn *Rag1*^{tm1Mom}/J (OTII)	Barnden et al.[89]	The Jackson Laboratory
C57BL/6-Tg(TcraTcrb)1100Mjb/J (OTI)	Hogquist et al.[90]	The Jackson Laboratory
B6.129P2(SJL)-*Myd88*^{tm1Defr}Cg-Tg(Itgax-cre) 1-1Reiz/J (MyD88^{DCD11c})	Caton et al.[91] and Hou et al.[92]	The Jackson Laboratory
B6.SJL-*Ptprc*^a *Pepc*^b/Boy/J (CD45.1)	Shen et al.[93]	The Jackson Laboratory
C57BL/6-pIgR^{tm}/J (pIgR-/-)	Shimada et al.[94]	The Jackson Laboratory
B6.Cg-Tnfrsf11a^{tm1.1lrw}/J-Tg (Vil1-cre)997Gum/J (RANK^{DIEC})	Rios et al.[45]	The Jackson Laboratory
B6(Cg)-Ifnar1^{tm}/J-Tg(Itgax-cre) 1-1Reiz/J (IFNAR^{DCD11c})	Caton et al.[91] and Kamphuis et al.[95]	The Jackson Laboratory
B6.129P2(Cg)-*Cx3cr1*^{tm1Litt}/J (CX3CR1-GFP)	Jung et al.[96]	The Jackson Laboratory
Oligonucleotides		
5'-GCTGCCTCCCGTAGGAGT-3'	IDT	Eub338 3' and 5' AF647 labeled
5'-CCTACGGGNGGCWGCAG-3' (16S_341_F)	Klindworth et al.[97]	16S_341_F
5'-GACTACHVGGGTATCTAATCC-3' (16S_805_R)	Klindworth et al.[97]	16S_805_R

(*Continued on next page*)

Continued

REAGENT or RESOURCE	SOURCE	IDENTIFIER
Ccl9	Thermofisher Scientific	Mm00441260_m1
Spib	Thermofisher Scientific	Mm03048233_m1
Gp2	Thermofisher Scientific	Mm00482557_m1
Intronic GAPDH	Thermofisher Scientific	Mm05724508-g1
Hprt	Thermofisher Scientific	Mm00446968_m1
Software and algorithms		
FlowJo v10	BD	RRID: SCR_008520
Seurat v3.1.0	Satija et al.[98]	https://satijalab.org/seurat/
Prism v9	GraphPad Software	RRID: SCR_002798
Cell Ranger v2.1.1	10x Genomicx	https://support.10xgenomics.com/single-cell-gene-expression/software/release-notes/2-1
DeqMS v1.8.0	N/A	https://github.com/yafeng/DEqMS
Monocle v2.12.0	Trapnell et al.[99]	https://www.bioconductor.org/packages/release/bioc/html/monocle.html
BOTA v0.1.0	Graham et al.[35]	N/A
MEGAhit v1.2.9	Li et al.[100]	https://kbase.us/applist/apps/MEGAHIT/run_megahit/release
PROKKA v1.13	Seemann et al.[101]	https://github.com/tseemann/prokka/releases
Kofamscan v1.3.0	Aramaki et al.[102]	https://github.com/takaram/kofam_scan
Trimmomatic v0.36	Bolger et al.[103]	http://www.usadellab.org/cms/?page=trimmomatic
BBmap 11-06-2018	Bushnell[104]	https://jgi.doe.gov/data-and-tools/software-tools/bbtools/bb-tools-user-guide/bbmap-guide/
BBsplit 11-06-2018	Bushnell[104]	https://github.com/BioInfoTools/BBMap/blob/master/sh/bbsplit.sh
iTOL v6.5	Letunic et al.[105]	https://itol.embl.de/

RESOURCE AVAILABILITY

Lead contact
Further information and requests for resources and reagents should be directed to and will be fulfilled by the lead contact, Mathias W. Hornef (mhornef@ukaachen.de).

Materials availability
Material transfer agreements with standard academic terms will be established to document reagent sharing by the lead contact's institution.

Data and code availability
- scRNAseq data are deposited with the National Center for Biotechnology Information Gene Expression Omnibus (GEO) under the accession numbers GSE188714.
- Metagenomic data are deposited under the NCBI-BioProject accession number PRJNA794356: https://www.ncbi.nlm.nih.gov/bioproject/PRJNA794356.
- Any additional information required to reanalyze the data reported in this paper is available from the lead contact upon request.
- This paper does not report original code.

EXPERIMENTAL MODEL AND SUBJECT DETAILS

Animals
All animal experiments were performed in compliance with the German animal protection law (TierSchG) and approved by the local animal welfare committees, the Landesamt für Natur, Umwelt und Verbraucherschutz, North Rhine Westfalia (84-02.04.2015.A063 and 84-02.04.2016.A207) and Regierungspräsidium Freiburg, Freiburg (X-20/05F). C57BL/6 wild-type (WT), B6.Cg-Tg(TcraTcrb)

425Cbn *Rag1*[tm1Mom]/J (OTII), C57BL/6-Tg(TcraTcrb)1100Mjb/J (OTI), B6.129P2(SJL)-*Myd88*[tm1Defr]Cg-Tg(Itgax-cre)1-1Reiz/J (MyD88[ΔCD11c]), B6.SJL-*Ptprc*[a] *Pepc*[b]/Boy/J (CD45.1), C57BL/6-pIgR[tm]/J (pIgR-/-), B6.Cg-Tnfrsf11a[tm1.1Irw]/J-Tg(Vil1-cre)997Gum/J (RANK[ΔIEC]), B6(Cg)-Ifnar1[tm]/J-Tg(Itgax-cre)1-1Reiz/J (IFNAR[ΔCD11c]) and B6.129P2(Cg)-*Cx3cr1*[tm1Litt]/J (CX3CR1-GFP) mice were bred locally and held under specific pathogen–free (SPF) or germ-free (GF) conditions at the Institute of Laboratory Animal Science at RWTH Aachen University Hospital. C57BL/6NTac wildling mice were created through inverse germ-free rederivation as previously desribed,[38] housed as well as bred locally at the animal facility of the Medical Center – University of Freiburg, Germany. C57BL/6NTac murine pathogen free (MPF) control mice were originally purchased from Taconic Biosciences, subsequently bred locally and housed under SPF conditions at the animal facility of the Medical Center - University of Freiburg, Germany. Wildlings and C57BL/6NTac MPF mice were age matched for all experiments.

In vivo models

For R848 administration, PND11 and adult mice were administered with 0.4 μg/g body weight (b.w.) R848 by intragastric gavage. For the OTI/OTII transfer, 1-2x10^5 eF670 marked OTI or OTII cells/g b.w. were transferred into PND11 and adult mice i.p. and OVA was administered 24 h later by intragastric gavage at 2 mg/g body weight 48 h after OVA administration, the proliferation of the transferred T cells was assessed. In experiments involving R848, R848 was orally gavaged 4-5 h after OVA at 0.4 μg/g b.w. For exposure of neonatal mice to the adult/weaning enteric microbiota, small intestine, caecum, and colon of one adult animal or two PND21-22 animals were opened longitudinally and flushed with 3-5 mL sterile PBS per animal for 5 min. under gentle agitation. Tissues were removed and clumps were suspended by vigilant pipetting. Large matter was removed by brief centrifugation at 300g for 30s and the supernatant was collected. Aliquots of adult intestinal content were stored at -20°C for single use and administered daily by intragastric gavage to neonatal mice starting at PND3-10 for T cell activation analysis or PND9-11 for the MNP analysis. For administration of *B.fragilis* (mix of strains CLA-KB-H83 and CLA-JM-H48) 5x10^9 bacterial cells from frozen stocks were administered by oral gavage at PND9-11. *E.coli* OMVs were prepared as described by Erttman et al., and gavaged 25μg were administered by oral gavage. Flagellin (from S.*Typhimurium*, ultrapure, Invivogen) and recombinant RANKL (Biomol) were injected i.p. at 2μg and 10μg at PND9-11, respectively. For the administration of fluorescent beads, 5x10^11 yellow-green fluorescent 100 nm beads/g b.w. (Polysciences) were administered by intragastric gavage to PND11 and adult mice and PP were examined 6 h later.

Vaccination against *S.*Typhiumrium/ *S.*Typhimurium infection

The vaccination protocol from Moor et al.[44] was adapted. *Salmonella* Typhimurium (STm) (SL1344) was grown in 500 mL at 37°C and 200 rpm to late stationary phase, harvested by centrifugation (3000 xg, 15 min., 4°C) and resuspended at 10^9-10^10 CFU/mL in PBS. Bacterial suspensions were incubated in 10 mL aliquots in 50 mL tubes with 0.04% peracetic acid (PAA) (Sigma) for 1 h at RT, centrifuged at 3000 xg for 10 min. and resuspended at 10^11 particles/ mL. 100 μl of the suspension was plated to verify complete inactivation. Mice were orally gavaged with 4x10^9 particles PAA STm/g b.w. ± 0.4 μg/b.w. R848 at PND7 and 14 and with PAA STm but no R848 at PND21. Adult mice were pretreated with streptomycing and orally infected with 10^3 CFU STm. Serum and SI wash and colonic LP cells were collected 24 hours post infection. Neonatal mice were infected orally with 2x10^3 CFU STm.

METHOD DETAILS

Isolation of PP cells

For neonatal PP a dissection microscope was used. PP were excised, counted and digested using 0.2 mg/mL Liberase TH/DNAse I for 45 min at 37°C and then dissociated by vigorous pipetting. Myeloid cells were positively enriched using CD11c MicroBeads (Miltenyi). OTI and OTII cells were isolated from lymph nodes and digested using 0.2 mg/mL Liberase TH/DNAse I for 45 min at 37°C and then dissociated by vigorous pipetting. OTI cells were then further enriched using a naïve CD8^+ T cell isolation kit (Miltenyi).

Flow cytometry and cell sorting

Single cell suspensions were blocked with anti-mouse CD16/32 (clone 93, Biolegend, 1:200 dilution) and stained with fluorescently labeled antibodies for 20-40 min. at 4°C. Antibodies were used at a 1:200 dilution unless stated otherwise. CCR7 surface staining was incubated at room temperature for 45 min. at a dilution of 1:50 prior to surface staining with the other antibodies. To determine coating of *Salmonella* with specific immunoglobulins from serum and small intestinal washes the protocol published by Moor et al.[44] was used. Blood was collected into clotting activating gel tubes (Sarstedt), incubated 15-30 min. at RT and centrifuged at 16000 xg for 15 min.; serum was stored at -20°C until further use. Small intestines were opened longitudinally, suspended in sterile PBS for 5 min., and vortexed. The tissue was removed and the SI wash was centrifuged at 16000 xg for 10 min.; supernatants were stored at -20°C until further use. Serum and SI washes were inactivated at 56°C for 30 min. and centrifuged at 16000 xg for 10 min. *Salmonella* Typhimurium (SL1344) were grown to late stationary phase in liquid medium, pelleted at 3000 xg at 4°C for 10 min., washed in 0.4 μm filtered PBS, and resuspended at 10^7 CFU/mL in 0.4 μm filtered 3%FCS/PBS. Sera and SI washes serially diluted (1:2) with an initial dilution of 1:3 and undiluted, respectively. 25 μl of bacteria were incubated with 25 μl of serum/SI wash for 1 h at 4°C, washed twice with 200 μL 0.4 μm filtered 3% FCS/PBS, stained with fluorescently labeled antibodies for 1 h at 4°C and washed before acquisition.

Following antibody clones (Biolegend) were used: anti-CD11b (clone M1/70), anti-CD11c, anti-CD4 (clone RM4-5), anti-CD44 (clone IM7), anti-CD45R/B220 (clone RA3-6B2), anti-CD86 (clone GL1), anti-IA/IE (clone M5/114.15.2, 1:400), anti-XCR1 (clone ZET), anti-BST2 (clone 927), anti-CCR7 (clone 4B12), anti-CD8a (clone 53-6.7), anti-CD19 (clone 6D5), anti-CD45 (clone 30-F11),

anti-CD45.1 (clone A30), anti-CD45.2 (clone 104), anti-SIRPa (clone P84), anti-CD74 (clone In1/CD74), anti-mouse IgG1 (clone RMG1-1, 1:40), anti-mouse IgA (clone C10-3, 1:50), anti-mouse IgM (clone RMM-1), anti-RORgt (clone B2D), anti-TCRb (clone H57-597), anti-TCRVa2 (clone 20.1), anti-GL7 (clone GL7), anti-B220 (clone RA3-6B2), anti-CD19 (clone 6D5), anti-CD3 (clone 17A2), anti-CD64 (clone X54-5/7.1), anti-FAS (clone Jo2, BD opti build). Homemade PLET1 antibody was provided by C.Ruedl and conjugated to AF647. Dead cells were stained with 7-AAD (Biolegend) or ZOMBIE NIR (Biolegend). Countbrite counting beads (Biolegend) were added to the FACS samples to assess the absolute cell numbers. Cells were acquired on a BD LSR Fortessa or a Cytek Aurora. Cell sorting was carried on a FACS ARIA II (BD) equipped with a 100 mm nozzle using BD FACS DIVA software. Final analysis was performed using FlowJo (V 10, BD).

DC OTII co-culture and T helper cytokine induction
PP MNP (MHCII$^+$CD11c$^+$CD45$^+$live) from PND11 and adult wild type mice (pooled litter, 4 adult animals per biological replicate) and OTII (CD4$^+$live) were FACS sorted and co-cultured at a ratio of 1:5 in IMDM 10% FCS, 1% penicillin and streptomycin (GIBCO), 1% L-glutamine (GIBCO) and 5 nM 2-mercaptoethanol (Carl-Roth) in the presence of 1 mg/mL OVA for 5 days. Supernatants were analyzed using the Legendplex mouse T helper cytokine panel version 3 (Biolegend) according to the manufacturer's instructions. Independent experiments were pooled after normalization.

Quantification of 16S rRNA gene copy numbers
The 16S rRNA gene copy numbers were determined in total homogenized small intestinal and colonic tissue samples of C57BL/6J wildtype mice collected at 1, 7, 14, 28, and 56 days after birth (n = 6/age group) and described previously.[67] Total DNA was isolated from approximately 200 mg frozen tissue by repeated bead-beating combined with chemical lysis and column-based purification using the QIAamp DNA Stool Mini Kit (Qiagen, Hilden, Germany) according to the manufacturer's instructions.[106] Subsequently, the PCR primers 5′-CCTACGGGNGGCWGCAG-3′ (16S_341_F) and 5′-GACTACHVGGGTATCTAATCC-3′ (16S_805_R) were used for amplification.[97] The real-time PCR was performed on a MyiQTM System (BioRad, USA) in a reaction-volume of 25 μl with 12.5 μl iQTM SYBR Green (Biorad), 2 μl template DNA and 0.75 μl primers (10 μM). The cycling conditions were 95 °C for 3 min. followed by 35 cycles of 95 °C for 15 s; 55 °C for 20 s and 72 °C for 30 s. Total 16S gene copy numbers were calculated by comparing the CT value to a standard curve with known concentrations of a plasmid encoding the 16S rDNA gene target sequence of *E.coli*. Tissues from germ free animals were used as negative controls, in which no specific PCR product was detected.

Quantification of bacteria by anaerobic culture
Small intestines were opened longitudinally, quickly transferred to Hungate tubes containing anaerobic PBS (0.05% L-cysteine, 0.02% DTT; gas mixture of 6% CO_2, 4.7% H_2 in N_2) with ~10 glass beads and vortexed. To ensure anaerobic conditions, the supernatant was transferred into another Hungate tube containing anaerobic PBS (0.05% L-cysteine, 0.02% DTT) using a sterile syringe fitted with a needle to inoculate through the rubber stopper of the Hungate tube. The suspension was plated onto tryptone soy agar plates with 5% sheep blood (Oxoid) in an anaerobic workstation (MBRAUN, Garching, Germany; same gas mixture as above). All materials were brought into the workstation at least 24h prior to work. CFU were quantified after 24h of incubation at 37 °C.

Immunofluorescence and confocal microscopy
For spectral confocal imaging CX$_3$CR1-GFP$^{+/-}$ reporter mice were used. PP were excised and fixed using Antigenfix for 45 min. at 4°C and incubated in 30% sucrose/PBS until saturated. Then, they were embedded in OCT compound as part of intestinal tube in an upright position, frozen over liquid nitrogen and stored at -80°C. Sections were cut at 10μm thickness and slides were stored at -20°C. After permeabilization and unspecific binding site blocking with PBS containing 0.5% saponin, 2% bovine serum albumin, 1% fetal calf serum, and 1% donkey serum for 30 minutes, sections were labeled overnight at 4°C with primary antibodies followed by washing in PBS before incubation for 1 hour at room temperature with secondary antibodies. Sections were then washed and blocked with sera of primary antibody species for 30 minutes, before staining in the same blocking buffer with fluorochrome-coupled antibodies for 1 hour. Slides were mounted in ProLong Gold and observed with a Zeiss LSM 780 confocal microscope using the spectral imaging mode.[107] For FISH staining tissues were fixed using methacarn to ensure the preservation of the mucus structure and subsequently paraffin embedded. Sections were deparaffined using successive xylene washes and ethanol washes (95%, 90%) before being rehydrated with ddH20. Sections were stained for commensal bacteria using the eubacterial FISH probe Eub338 (GCT GCC TCC CGT AGG AGT) labelled with AF647 at 100nM in hybridization buffer (0.9M NaCl, 20-mM Tris-Hcl pH 7.2 0.1%SDS Tris) at 50°C overnight. Slides were washed with prewarmed wash buffer (0.9M NaCl, 20-mM Tris-Hcl pH 7.2) prior to Hoechst 33342 (10ug/mL) nucleic acid staining. Slides were mounted using ProLong Antifade Gold and imaged using a Nikon 90i at the University of Pittsburgh Center for Biological Imaging.

Quantification of the CD11c signal distribution in PP
In a first instance all images were manually segmented by encircling each follicle individually with a polygon. This polygon mask served, together with the image, as basis for further processing steps. To determine the distribution of the CD11c signal with respect to the distance to the surrounding shape the following steps were performed: First, the image was filtered with a Gaussian kernel (σ=9, filter size: 201x201) to achieve a smoother surface and to account for the sparse distribution of positive cells within the image. Next, mean pixel intensities were computed within rings with a specified minimum and maximum distance from the masks' contour.

This was obtained using morphological erosion with circular structuring elements of different diameters. To measure the occurrence of the CD11c signal with respect to distance to the contour, we extracted these mean values in non-overlapping, consecutive rings within the whole mask as illustrated in Figure 3B. The thickness (diameter) of each ring was set to 5 pixels to achieve a good trade-off between resolution and smoothness. The center circle was not considered for further processing since it can become arbitrarily small leading to inaccurate measurements. With the obtained mean values, we fit a first order polygon and used the slope Δ as a descriptor for each follicle. The descriptor was normalized for the size of the mask by multiplying the slope with the number of rings.

Single cell RNA sequencing and analysis

Pooled cells from a litter of neonatal mice (5-8 animals) or 3 adult mice were used and samples were analyzed in biological duplicates for the PND11 vs. adult PP MNP experiment and as single samples for the R848 stimulation experiment. MACS enriched cells isolated from PP were subjected to FACS sorting as CD11c+MHCII+CD45+live+IgA-TCRb- and further processed using the Chromium Single Cell 3' v2 kit (10xGenomics) according to the manufacturer's protocol. After library generation, sequencing was performed on a NextSeq 550 (IZKF genomics facility of the RWTH Aachen University, Aachen, Germany). Sequencing was performed on Illumina NextSeq 550 (paired-ends, 2×75 bp). With default parameters, we used Cell Ranger (version 2.1.1) to align reads to the mouse genome mm10. Following that, we utilized Seurat (v3.1.0)[98] to achieve a high-level analysis of the scRNA-seq data. Cells with high mitochondrial ($\geqq 10\%$) and ribosomal ($\geqq 25\%$) gene content, as well as cells with $\geqq 30.000$ UMIs having an increased probability to represent doublets and cells with $\leqq 30$ detected genes were excluded from further analysis. We used Seurat to regress out cell cycle, mitochondrial, ribosomal, and UMI counts and performed a log-normalization of read counts. In a second step contaminant cell types (B cells, Cd19; pDCs, Siglec; villus macrophages; Fcgr1 (the latter only for the data set examining naïve PND11 vs. adult MNP)) were removed. After quality control and contaminant removal 3659 and 10756 cells were analyzed and depicted in the UMAPs in Figures 1E and 6H, respectively. Canonical correlation analysis (CCA) based on the first 15 CCs was used to combine samples from R848 and PBS experiments.[108] Unsupervised clustering was performed using a shared nearest neighbors graph with a resolution of 0.8 and k = 15. The following parameters were used to build UMAP representations: min dist = 0.3, max.dim = 2, seed.use = 36). To determine cluster specific markers, we implemented the FindMarkers gene function with an adjusted p value of 0.05. Differential gene expression analysis was performed with Seurat using the Wilcoxon test. Next, we used monocle (version 2.12.0)[99] in the integrated data to reconstruct cell development trajectories. For the reconstruction of cell development trajectories, we employed the 1000 most relevant genes identified by Monocle's unsupervised feature selection approach (dpFeature). The root of the trajectory was defined choosing the branch with the highest S-score, which also correlated with the expression of stemness-associated genes such as *Birc5*. For the PND11 PBS vs. PND11 R848 and adult PBS vs. adult R848 scRNA-seq data set data integration was performed by anchors identification based on the results of CCA analysis. The first 20 CCs were used for the anchor identification and first 20 PCs from PCA analysis were used for UMAP representation. For clustering resolution was set to 0.5. For the analysis of commonly regulated genes in PND11 vs. Adult and PND11 PBS vs. R848 qDC2 Gene Set Enrichment Analysis (GSEA) via gseGO function and the compareClusters function from clusterProfiler(cite here) (version 4.6.0) package was performed. Both sets were further sub-divided on average log_FC values - genes with average log_FC > 0 were considered to be Upregulated while those with average log_FC < 0 were considered to be Downregulated. The enrichGO function via the fun parameter of the compareClusters function was used to carry out enrichment analysis of respective upregulated and downregulated genes and the resulting shared set of GO terms and associated genes were depicted using a cnet plot. Comparative GO term enrichment was further carried out using the REVIGO pipeline.[109] Pseudobulk analysis against the ImmGen clusters was carried out as previously described.[110] Raw data were deposited under GEO accession number GSE188714.

Shotgun metagenomic sequencing

DNA for the metagenomic analysis was isolated using a modified protocol according to Godon et al.[111] Snap frozen samples were mixed with 600 μl stool DNA stabilizer (Stratec Biomedical), thawed, and transferred into sterile 2-mL screw-cap tubes containing 500 mg 0.1 mm (diameter) silica/zirconia beads. 250 μl 4 M guanidine thiocyanate in 0.1 M Tris (pH 7.5) and 500 μl 5 % N-lauroyl sarcosine in 0.1 M PBS (pH 8.0) were added. Samples were incubated at 70 °C and 700 rpm for 60 min. A FastPrep® instrument (MP Biomedicals) cooled with dry ice was used for cell disruption (3 x 40 s at 6.5 M/s). Subsequently, 15 mg polyvinylpyrrolidone (PVPP) was added and samples were vortexed, followed by 3 min. centrifugation at 15000 xg and 4°C. Approximately 650 μl of the supernatant was transferred into a new 2 mL tube, which was centrifuged for 3 min. at 15000 xg and 4°C. Afterwards, 500 μl of the supernatant were transferred into a new 2 mL tube and 50 μg of RNase was added. After incubation at 37 °C and 700 rpm for 20 min., the gDNA was isolated using the NucleoSpin® gDNA Clean-up Kit from Macherey-Nagel according to the manufacturer's protocol. DNA was eluted from columns twice using 40 μl elution buffer and the concentration was determined using a NanoDrop® (Thermo Scientific). Samples were stored at -20 °C.

Sequencing of the metagenomic DNA was performed as follows: mechanical shearing of 600 ng DNA to a size of 200 bp (200 s, peak incident power: 75 W, duty factor: 10%, cycles per burst: 200) was performed using a Covaris M220. Subsequently the libraries were prepared with the NEBNext® Ultra II DNA Library Prep Kit for Illumina® (NEB, USA) according to the manufacturer's protocol. The PCR enrichment of adaptor-ligated DNA was conducted with 7 cycles and NEBNext® Multiplex Oligos for Illumina® (NEB, USA) for single-end barcoding. Size selection and clean-up of adaptor ligated DNA was conducted using AMPure beads (Beckman

Coulter, USA). The quality (TapeStation, Agilent Technologies, USA) and quantity (Quantus, Promega, USA) of the resulting libraries was checked at the IZKF Core Facility (UKA, RWTH Aachen University) prior to sequencing on a NextSeq500 (Illumina, USA) with a NextSeq500 High Output Kit v2.5 (300 Cycles).

Metagenomic data analysis

For quality control, the metagenomic reads were first trimmed using Trimmomatic[103] using a sliding window of 5:20, minimum length of 50, trailing of 3, leading of 3 and illumine clipping values of 2:30:10. Host reads were removed using BBmap[104] to map the reads against the genome of *Mus musculus* GRCm38. Alignment was done using a minimum ratio of 0.9, maximum indel of 3, band width ratio of 0.16, band width of 12, minimum hits of 2 with at least 25 consecutive matches using a kmer length of 14. The first 10bp on each read before mapping and regions with an average score below 10 were also trimmed but undone after mapping (untrim).

The host-filtered reads of the metagenomic DNA were then assembled using MEGAhit[100] using a kmer list of 21,27,33,37,43,55,63,77,83,99, with a minimum multiplicity for filtering kmers of 5. PROKKA was used to predict the proteome from the assembled contigs using default options.[101] The predicted proteome was functionally annotated against the KEGG database using Kofamscan.[102]

Host-filtered reads were then aligned to the iMGMC non-redundant collection of metagenome-assembled genomes (MAGs)[34] using BBsplit[104] with a minimum identity of 90% to produce a coverage statistics file which was converted into TPM via the make-TPMfromCovStats.sh script from the iMGMC best-practices repository. The TPM values were used to calculate the minimal number of species that covered the maximal amount of the data based on the knee point, implemented in python using the Kneed module.[112] Only MAGs with a TPM value >100 in >2 samples were retained for further analysis.

A phylogenomic tree of the 153 iMGMC-derived MAGs was generated using their predicted proteomes in Phylophlan3 v3.0.60.[113] Diversity was set as high using the 'supermatrix_aa.cfg' config file. The tree was visualized in iTOL.[105] Raw data were deposited under BioProject accession number PRJNA794356.

Antigenic peptide prediction from metagenomic data using BOTA

The proteins encoded on the 153 MAGs recovered from iMGMC were predicted using PROKKA v1.14.6.[101] The genome, predicted proteome and general features were used as input for BOTA v0.1.0[35] using the H-2-IAb model for MHC class II (allele IA) antigen prediction.

Metaproteomic analysis

For metaproteome analysis, samples were dissolved in 500 μl SDS lysis buffer (0.29 g NaCl, 1M Tris-HCL pH=8, 5M EDTA pH=8, 0.4g SDS in 100 mL water). Protein extraction was done by bead beating (FastPrep-24, MP Biomedicals, Sanra Ana, CA, USA; 5.5 ms, 1 min., 3 cycles) followed by ultra-sonication (UP50H, Hielscher, Teltow, Germany; cycle 0.5, amplitude 60%) and centrifugation (10,000 xg, 10 min.). The protein lysate was loaded on a SDS-gel and run for 10 min. The gel piece was cut, washed and incubated with 25 mM 1,4 dithiothreitol (in 20 mM ammonium bicarbonate) for 1 h and 100 mM iodoacetamide (in 20 mM ammonium bicarbonate) for 30 min., destained, dehydrated and proteolytically cleaved overnight at 37 °C with trypsin (Promega). The proteolytically cleaved peptides were extracted and desalted using ZipTip μC18 tips (Merck Millipore, Darmstadt, Germany). The peptide lysates were re-suspended in 15 μl 0.1% formic acid and analysed by nanoliquid chromatography mass spectrometry (UltiMate 3000 RSLCnano, Dionex, Thermo Fisher Scientific). Mass spectrometric analysis of eluted peptide lysates was performed on a Q Exactive HF mass spectrometer (Thermo Fisher Scientific) coupled with a TriVersa NanoMate (Advion, Ltd., Harlow, UK). Peptide lysates were injected on a trapping column (Acclaim PepMap 100 C18, 3 μm, nanoViper, 75 μm x 2 cm, Thermo Fisher Scientific) with 5 μl/min. using 98% water/2% ACN 0.5% trifluoroacetic acid, and separated on an analytical C18 column (Acclaim PepMap 100 C18, 3 μm, nanoViper, 75 μm x 25 cm, Thermo Fisher Scientific) with a flow rate of 300 nl/min. The mobile phase was 0.1% formic acid in water (A) and 80 % ACN/0.08 % formic acid in water (B). Full MS spectra (350–1,550 m/z) were acquired on the Orbitrap at a resolution of 120,000 with an automatic gain control (AGC) target value of 3×10^6 ions. Data resulting from LC-MS/MS measurements were analyzed with the Proteome Discoverer (v.2.4, Thermo Fischer Scientific) using SEQUEST HT. Protein identification was performed using a self-built reference database downloaded from UniProt (reference numbers: UP000008827.fasta, UP000019116.fasta, UP000007305.fasta and the predicted proteome from the combined metagenomic assembly). Searches were conducted with the following parameters: Trypsin as enzyme specificity and two missed cleavages allowed. A peptide ion tolerance of 10 ppm and an MS/MS tolerance of 0.05 Da. As modifications, oxidation (methionine) and carbamidomethylation (cysteine) were selected. Peptides that scored a q-value >1% based on a decoy database and with a peptide rank of 1, were considered identified. For the differential analysis of the proteomics data the R package DeqMS 1.8.0 (https://doi.org/10.1074/mcp.TIR119.001646) was used. For each group (PND11 and adult), proteins with valid quantification in at least half of the samples (3/6) were included.

QUANITIFICATION AND STATISTICAL ANALYSIS

The Mann-Whitney U test was used to compare two groups, the Kruskall-Wallis with Dunn's multiple comparison was used to compare multiple groups and one variable, 2-way-ANOVA with Bonferroni's multiple comparison test was used to compare multiple groups and two variables. Statistical tests were carried out using Graphpad Prism and $p < 0.05$ was considered significant. The number of biological replicates analyzed and the statistical test used are indicated in the respective figure legends. ns, not significant; *, $p < 0.05$; **, $p < 0.01$; ***, $p < 0.001$, ****, $p < 0.0001$.